High Resolution 3D Winds Derived from a Modified WISSDOM Synthesis Scheme using Multiple Doppler Lidars and Observations

Chia-Lun Tsai[1], Kwonil Kim[1], Yu-Chieng Liou[2], and GyuWon Lee*[1]

[1]Department of Astronomy and Atmospheric Sciences, Center for Atmospheric REmote sensing (CARE), Kyungpook National University, Daegu, South Korea

[2]Department of Atmospheric Sciences, National Central University, Jhongli, Taiwan

---

* Corresponding author: Prof. GyuWon Lee, E-mail: gyuwon@knu.ac.kr

Abstract

A WISSDOM (Wind Synthesis System using Doppler Measurements) synthesis scheme was developed to derive high-resolution 3-dimensional (3D) winds under clear-air conditions. From this variational-based scheme, detailed wind information was obtained from scanning Doppler lidars, automatic weather stations (AWS), sounding observations, and local reanalysis datasets (LDAPS, Local Data Assimilation and Prediction System), which were utilized as constraints to minimize the cost function. The objective of this study is to evaluate the performance and accuracy of derived 3D winds from this modified scheme. A strong wind event was selected to demonstrate its performance over complex terrain in Pyeongchang, South Korea. The size of the test domain is 12×12 km^2 extended up to 3 km height mean sea level (MSL) with remarkably high horizontal and vertical resolution of 50 m. The derived winds reveal that reasonable patterns were explored from a control run, as they have high similarity with the sounding observations. The results of intercomparisons show that the correlation coefficients between derived horizontal winds and sounding observations are 0.97 and 0.87 for u- and v-component winds, respectively, and the averaged bias (root mean square deviation, RMSD) of horizontal winds is between −0.78 and 0.09 (1.7~~72~~ and 1.65) m s^{-1}. The correlation coefficients between WISSDOM-derived winds and lidar QVP (quasi-vertical profile) are 0.84 and 0.35 for u- and v-component winds, respectively, and the averaged bias (RMSD) of horizontal winds is between 2.83 and 2.26 (3.69 and 2.92) m s^{-1}. The statistical errors also reveal a satisfying performance of the retrieved 3D winds; the median values of wind directions are −5~5 (0~2.5) degrees, the wind speed is approximately −1~3 m s^{-1} (−1~0.5 m s^{-1}) and the vertical velocity is –0.2~0.6 m s^{-1} compared with the lidar QVP (sounding observations). A series of sensitivity tests with different weighting coefficients, radius of influence (RI) in interpolation and various combination of different datasets were also performed~~.,~~ ~~Tand t~~he results indicate that the present setting of the control run is the optimal reference to WISSDOM synthesis in this ~~event~~event and will help verify the impacts against various scenarios and observational references in this area~~.~~.

1. Introduction

In the past few decades, many practical methods have been developed to derive wind information by using meteorological radar data (Mohr and Miller, 1983, Lee et al., 1994, Liou and Chang, 2009, Bell et al. 2012). The derived winds substantially revealed reasonable patterns compared with conventional observations (such as surface stations, soundings, wind profiles, etc.) and models (Liou et al., 2014, North et al., 2017, Chen, 2019, Oue et al., 2019). Most comprehensive applications of the derived winds were adopted to document kinematic and precipitation structures associated with various weather systems or phenomena at different scales from thousands, hundreds, and a couple of kilometers, such as like cold fronts, typhoons, tropical cyclone rainbands, convective lines, and non-precipitation low-pressure systems (LPS) (Yu and Bond, 2002, Yu and Jou, 2005, Yu and Tsai, 2013, Yu and Tsai, 2017, Tsai et al. 2018, Yu et al., 2020, Cha and Bell, 2021, Tsai et al., 2022). In addition, the accuracy of 3D winds could be improved when increasing the numbers of Doppler radar because relatively fewer assumptions and more information can be included (Yu and Tsai 2010, Liou and Chang, 2009). Therefore, the retrieved schemes within multiple Doppler radars are a more popular way to obtain high-quality 3D winds and have been extensively applied to meteorological analyses.

The technique of velocity track display (VTD, Lee et al., 1994) and ground-based velocity track display (GBVTD, Lee et al., 1999) can derive the winds from single Doppler radar under some assumptions, as the wind patterns are generally uniform or axisymmetric rotational (Cha and Bell, 2021). More extended techniques based on VTD and GBVTD have also been applied to increase the quality of derived wind data, and such techniques include Extended-GBVTD (EGBVTD, Liou et al., 2006) and generalized velocity track display (GVTD, Jou et al., 2008). However, winds usually present nonuniform patterns and fast-evolving characteristics in most mesoscale weather systems and microscale phenomena, and complete and detailed winds are still difficult to resolve by these techniques. Most developed techniques are bBased on the contexts of weaknesses from the above schemes on the wind retrievals. Instead of a single Doppler radar,

68   multiple Doppler can retrieve better quality 3D winds with relativity fewer assumptions because

69   they provide sufficient radial velocity measurements and wind information with wider coverage

70   in the synthesis domain.

71   Cartesian Space Editing, Synthesis, and Display of Radar Fields under Interactive Control

72   (CEDRIC, Mohr and Miller, 1983) is a traditional package used to retrieve 3D winds by dual-

73   Doppler radar observations. This scheme usually determines the horizontal winds by using two

74   radars, and the vertical velocity can be obtained by variational adjustment with anelastic

75   continuity equation. Spline Analysis at Mesoscale Utilizing Radar and Aircraft Instrumentation

76   (SAMURAI) software is another way to retrieve 3D winds (Bell et al., 2012); this scheme is a

77   kind of variational data assimilation that adopts multiple radars. Recently, Tsai et al. (2018)

78   utilized the measurements of six Doppler radars to document precipitation and airflow structures

79   over complex terrain on the northeastern coast of South Korea via WISSDOM (Wind Synthesis

80   System using Doppler Measurements). Liou and Chang (2009) is t~~T~~he first purposes ~~and details~~

81   ~~of~~ of this algorithm~~s can be found in Liou and Chang (2009).~~. Furthermore, they p~~P~~erform~~eding~~

82   immersed boundary method (IBM, Tseng and Ferziger, 2003) in WISSDOM, and its scientific

83   applications were ~~clearly~~ documented in Liou et al. (2012), and Liou et al. (2016), respectively.

84   Since one of the advantages of WISSDOM is that it considers the orographic forcing on Cartesian

85   coordinates by applying the IBM, higher quality 3D winds can be derived well over terrain (Liou

86   et al., 2013, 2014, Lee et al., 2018).

87   Generally, radial velocity is measured by detecting the movement of precipitation particles

88   relative to the locations of Doppler radars; thus, there are no sufficient radial velocity

89   measurements under clear-air conditions. However, the winds in clear-air conditions usually play

90   an important role in the initiations of various weather systems and phenomena, such as downslope

91   winds, gap winds, and wildfires (Reed, 1931, Colle and Mass, 2000, Mass and Ovens, 2019, Lee

92   et al., 2020). Although surface stations, soundings, and wind profilers can measure winds under

93   clear-air conditions, relatively poor spatial coverage is still a problem for obtaining sufficient

94 wind information in certain local areas. Therefore, scanning Doppler lidars will be one approach

95 to obtain wind information under clear-air conditions. Päschke et al. (2015) assessed the quality

96 of wind derived by Doppler lidar with a wind profiler in a year trial, and the results showed good

97 agreement in wind speed (the error ranged between 0.5 and 0.7 m s^{-1}) and wind direction (the

98 error ranged between 5° and 10°). Bell et al. (2020) combined an intersecting range height

99 indicator (RHI) of six Doppler lidars to build "virtual towers" (such as wind profilers) to

100 investigate the airflow over complex terrain during the Perdigäo experiment. These virtual towers

101 can fill the gap in wind measurements above meteorological towers. The uncertainty of wind

102 fields is also reduced by adopting multiple Doppler lidars (Choukulkar et al., 2017), and a high

103 spatiotemporal resolution of derived wind is allowed to check small-scale rotors in mountainous

104 areas (Hill et al., 2010).

105 The original WISSDOM was designed to retrieve 3D winds based on Doppler radar

106 observations and background inputs combined with conventional observations and modeling.

107 However, the original WISSDOM only provided 3D winds under precipitation conditions., land

108 it cannot does not work well under clear-air conditions because the Doppler radar is cannot easily

109 to detect radial velocity without precipitation particles. To obtain high-quality 3D winds under

110 clear-air conditions for investigating the initiations of precipitation systems in advance of rain

111 and snow formatte, d. tThe radial velocity observed from the scanning Doppler lidars can be used

112 in modified WISSDOM. The results will allow, us to investigate the initiations of precipitation

113 systems in advance of rainfall and snowfall, which is the most importantan essential benefit rather

114 than Doppler radar in related research topics. Furthermore, the conventional observations and

115 modeling datasets were used as isolated constraints in the modified WISSDOM synthesis scheme.

116 One of the benefits of the isolated constraints is that it is easy to synthesize any kind of wind

117 information obtained from available datasets and give suitable weighting coefficients with

118 different constraints when they are processing the minimization in the cost function. Thus, more

119 reliable 3D winds in clear-air conditions were well derived from this modified WISSDOM

120 synthesis scheme.

121   The objective of this study is to modify the WISSDOM synthesis scheme based on the

122 original version to be a more flexible and useful scheme by adding any number of Doppler lidars

123 and conventional observations as well as modeling datasets. This modified WISSDOM will allow

124 us to obtain an exceedingly high spatial resolution of 3D winds (50 m was set in this study) under

125 clear-air conditions. A resolution of 50 m was chosen in this study, as the Doppler lidars'

126 respective horizontal resolution averages 40-60 m. ~~It is because the Doppler lidar had high spatial~~

127 ~~resolution in between 40 and 60 m horizontally, however, the Doppler radar had relatively low~~

128 ~~spatial resolution from approximately 100 to 1000 m.~~ A variety of adequate datasets were

129 collected during a strong wind event in the winter season during an intensive field experiment

130 ICE-POP 2018 (International Collaborative Experiments for Pyeongchang 2018 Olympic and

131 Paralympic winter games). In summary, the main goal of this study is to use Doppler lidar

132 observations to retrieve high-resolution 3D winds over terrain ~~under~~ with clear-air conditions via

133 WISSDOM. In this study, detailed principles of the modified WISSDOM and data

134 implementation are elucidated in the following sections. In addition, the modified WISSDOM

135 was performed to retrieve 3D winds over complex terrain under clear-air conditions in a strong

136 wind event. The reliability of the derived 3D winds was also evaluated and discussed with

137 conventional observations.

138 **2. Methodology**

139 **2.1 Original version of WISSDOM (WInd Synthesis System using DOppler Measurements)**

140   WISSDOM is a mathematically variational-based scheme to minimize the cost function, and

141 various wind-related observations can be used as one of the constraints in the cost function. The

142 3D winds were derived by variationally adjusted solutions to satisfy the constraints in the cost

143 function~~;~~, thus~~, the results of retrieved winds were~~this is ~~the~~a ~~analytic expression~~gradient decent

144 technique to converge toward a solution ~~in this scheme~~. The original version of WISSDOM

145 performed five constraints, including radar observations (i.e., reflectivity and radial velocity),

146 background (combined with automatic weather stations, sounding, model or reanalysis data),

147 continuity equation, vorticity equation, and Laplacian smoothing (Liou and Chang 2009). Liou

148 et al. (2012) applied the IBM in WISSDOM to consider the ~~affecting~~ effect ~~up~~on the nonflat

149 surface~~s.~~, ~~O~~one of the advantages ~~in~~ of IBM is providing realistic topographic forcing without

150 ~~the need to~~ chang~~ing~~e the Cartesian coordinate system into a terrain-following coordinate system.

151 More scientific documentation~~s~~ associated with the interactions between terrain, precipitation,

152 and winds in different areas can be ~~referred~~found in ~~to~~ Liou et al. (2016) for, Taiwan~~)~~, and in Tsai

153 et al. (2018) for, South Korea~~)~~. The cost function can be expressed as

$$J = \sum_{M=1}^{5} J_M, \tag{1}$$

155 where J_M is the different constraints. J_1 is the constraint related to the geometric relation

156 between radar radial Doppler velocity observations (V_r) and derived one from true winds $(\mathbf{V}_t =$

157 $u_t\mathbf{i} + v_t\mathbf{j} + w_t\mathbf{k})$ in Cartesian coordinates [eq. (2)]. Note that the $\mathbf{V}_t$ will be first guessed,

158 ~~random~~ resulting from the background of the sounding observations used in this study~~, modeling,~~

159 ~~or equal zero if there is not any information about wind in beginning~~.

$$J_1 = \sum_{t=1}^{2} \sum_{x,y,z} \sum_{i=1}^{N} \alpha_{1,i} \left(T_{1,i,t}\right)^2. \tag{2}$$

161 Since WISSDOM is a scheme that uses the 4DVAR approach, the variations between different

162 time steps (t) should be considered, and two time steps of radar observations were collected in

163 this constraint and all following constraints. The x, y, z indicates the locations of a given grid

164 point in the synthesis domain, and i could be any number (N) of radars (at least 1). The α_1 is

165 the weighting coefficient of J_1 (α_2 is the weighting coefficient of J_2 and so on). $T_{1,i,t}$ in eq.

166 (2) is defined as eq. (3):

167
$$T_{1,i,t} = (V_r)_{i,t} - \frac{(x - P_x^i)}{r_i} u_t - \frac{(y - P_y^i)}{r_i} v_t - \frac{(z - P_z^i)}{r_i} (w_t - W_{T,t}), \qquad (3)$$

168 $(V_r)_{i,t}$ is the radial velocity observed by the radar (i) at time step (t), P_x^i, P_y^i and P_z^i depict the

169 coordinate of radar i. The u_t, v_t and w_t $(W_{T,t})$ denote the 3D winds (terminal velocity of

170 precipitation particles) at given grid points at the time step t ; and $r_i =$

171 $\sqrt{(x - P_x^i)^2 + (y - P_y^i)^2 + (z - P_z^i)^2}$.

172   The second constraint is the difference between the background $(\mathbf{V}_{B,t})$ and true (derived)

173 wind field $(\mathbf{V}_t = u_t \mathbf{i} + v_t \mathbf{j} + w_t \mathbf{k})$, which is defined as

174
$$J_2 = \sum_{t=1}^{2} \sum_{x,y,z} \alpha_2 (\mathbf{V}_t - \mathbf{V}_{B,t})^2. \qquad (4)$$

175 There were several options to obtain background in the original version of WISSDOM. The most

176 popular background resource involves using sounding observations; however, it can only provide

177 homogeneous wind information for each level in WISSDOM with relatively coarse temporal

178 resolution (3- to 12-hour intervals). The other option is combining sounding observations with

179 AWS (automatic weather station) observations. Although the AWS provided wind information

180 with better temporal resolution (1-min), the data were only observed at the surface layer with

181 semirandom distributions. The last option is to combine sounding, AWS, modeling or reanalysis

182 datasets. However, various datasets with different spatiotemporal resolutions are not favorable

183 for appropriate interpolation of given grid points of WISSDOM synthesis, and the accuracy and

184 reliability of the background may have been significantly affected by such a variety of datasets.

185 Thus, these different observed or model data should be treated differently to minimize ~~the~~

186 uncertainties and improve ~~the~~ accuracy. ~~Thus~~Therefore, one of the improvements in the modified

187 WISSDOM is that these inputs were individually separated into independent constraints

188 ~~individually~~with flexible interpolation methods. In addition, individual constraints considered the

189 time if the temporal resolution of the inputs was equal to or higher than the time interval of the

190 WISSDOM outputs. Note that the sounding observations are still a necessary dataset because the

191 air density and temperature profile were used to identify the height of the melting level. In this

192 study, sounding winds were adopted to represent the background for each level and a constraint

193 at the same time; nevertheless, the AWS and reanalysis dataset are independent constraints in the

194 modified WISSDOM (details are provided in the following section).

195   The third, fourth and fifth constraints in the cost function are the anelastic continuity

196 equation, vertical vorticity equation and Laplacian smoothing filter, respectively. Equations (5),

197 (6) and (7) are denoted as follows:

198
$$J_3 = \sum_{t=1}^{2} \sum_{x,y,z} \alpha_3 \left[\frac{\partial(\rho_0 u_t)}{\partial x} + \frac{\partial(\rho_0 v_t)}{\partial y} + \frac{\partial(\rho_0 w_t)}{\partial z} \right]^2, \tag{5}$$

199
$$J_4 = \sum_{x,y,z} \alpha_4 \left\{ \frac{\partial \zeta}{\partial t} + \overline{\left[u \frac{\partial \zeta}{\partial x} + v \frac{\partial \zeta}{\partial y} + w \frac{\partial \zeta}{\partial z} + (\zeta + f) \left(\frac{\partial u}{\partial x} + \frac{\partial v}{\partial y} \right) + \left(\frac{\partial w}{\partial x} \frac{\partial v}{\partial y} - \frac{\partial w}{\partial y} \frac{\partial u}{\partial z} \right) \right]} \right\}^2, \tag{6}$$

200
$$J_5 = \sum_{t=1}^{2} \sum_{x,y,z} \alpha_5 [\nabla^2 (u_t + v_t + w_t)]^2. \tag{7}$$

201 ρ_0 in eq. (5) is the air density, and $\zeta = \partial v/\partial x - \partial u/\partial y$ in eq. (6). The main advantage is that

202 ~~the use of~~using vertical vorticity can provide further improvement ~~vement~~ in winds and

203 thermodynamic retrievals from a method named as Terrain-Permitting Thermodynamic Retrieval

204 Scheme (TPTRS, Liou et al. 2019).~~—~~

205 **2.2 The modified WISSDOM**

206   In addition to the five constraints in the original version, the modified WISSDOM synthesis

207 scheme includes three more constraints in the cost function. Thus, the cost function in the

208 modified WISSDOM was written as

209
$$J = \sum_{M=1}^{8} J_M. \tag{8}$$

210    $J_1 \sim J_5$ in (8) are the same constraints corresponding to equations (2)-(7). The main purpose

211 of this study is to retrieve 3D winds under clear-air conditions in which observational data are

212 relatively rare. Instead of the radial velocity $(V_r)_{i,t}$ observed from Doppler radars in eq. (3) in

213 original version of WISSDOM, the radial velocity observed from Doppler lidars was adopted in

214 the modified WISSDOM synthesis. In addition, if there were no precipitation particles under

215 clear-air conditions, the terminal velocity of precipitation particles $(W_{T,t})$ was set to zero in eq.

216 (3) in the modified WISSDOM. In this study, t~~T~~he time steps in WISSDOM ~~of this study~~ were

217 set by the synthesis time and 12 mins before the synthesis time due to the temporal resolution of

218 the ~~main~~ primary input lidar data ~~is~~ being 12 mins. Notably, relatively minor changes in

219 environmental conditions were assumed in WISSDOM due to the limitation on the coarse

220 temporal resolution from specific inputs. For example, the closest time step of a sounding

221 observation or LDAPS dataset was chosen regarding the synthesis time, and the time constrain

222 was set to be the same.

223   The sixth constraint is the difference between the derived wind fields and the sounding

224 observations ($\mathbf{V}_{S,t}$), as defined in (9):

225
$$J_6 = \sum_{t=1}^{2} \sum_{x,y,z} \alpha_6 \left(V_t - V_{S,t}\right)^2. \tag{9}$$

226 The sounding data in J_6 were interpolated to the given grid points near its tracks bearing on the

227 radius influence (RI) distance (the details are provided in Section 3.2.3). The main difference

228 between J_6 and J_2 is that the sounding data with various wind speeds and directions were used

229 as an observation for given 3D locations in J_6~~,~~ instead of the constraint of homogeneous

230 background winds (i.e., uniform wind speed and direction) for each level in the studied domain

231 in J_2. An additional benefit of J_6 is that any number of sounding observations can be efficiently

232 adopted in the WISSDOM synthesis domain. The seventh constraint represents the discrepancy

233 between the true (derived) wind fields and AWS ($\mathbf{V}_{A,t}$), as expressed in (~~8~~10):

234
$$J_7 = \sum_{t=1}^{2} \sum_{x,y,z} \alpha_7 \left(V_t - V_{A,t}\right)^2. \tag{\text{\textsterling}10}$$

235 Finally, the eighth constraint measures the misfit between the derived winds and the local

236   reanalysis dataset ($\mathbf{V}_{L,t}$), as defined in (~~9~~11):

$$J_8 = \sum_{t=1}^{2} \sum_{x,y,z} \alpha_8 \left(V_t - V_{L,t}\right)^2. \tag{$\cancel{9}$11}$$

238   In this study, various observations and reanalysis datasets were utilized as constraints in the cost

239   function of WISSDOM. The most important dataset is the radial velocity observed from Doppler

240   lidars, which can measure wind information with high spatial resolution and good coverage from

241   near the surface up to higher layers in the test domain. Sounding and AWS can provide horizontal

242   winds for background or to be included in the constraints. The local reanalysis datasets were

243   obtained from the 3DVAR Local Data Assimilation and Prediction System (LDAPS) data

244   assimilation system from the Korea Meteorological Administration (KMA). Since these datasets

245   have different coordinate systems and various spatiotemporal resolutions, additional procedures

246   are required before the synthesis. Detailed descriptions of the procedures are described in the next

247   section.

248   The high-quality synthesized 3D wind field from radar observations has been applied in

249   several previous studies such as those by Liou and Chang (2009), Liou et al. (2012, 2013, 2014,

250   2016), and Lee et al. (2017). The advantages and details of the WISSDOM can be found in Tsai

251   et al. (2018). Although ~~there were quite a few~~several studies have ~~by using~~used Doppler radar in

252   WISSDOM, this study is the first time to apply ~~the~~ Doppler lidar data in WISSDOM. This

253   modified WISSDOM synthesis scheme has also been applied in the analysis related to the

254   mechanisms of orographically induced strong wind on the northeastern coast of Korea (Tsai et

255   al., 2022). In contrast to~~different view standing from~~ previous studies, this study provides clear

256   context, detailed procedures, reliability, and the limitations of the modified WISSDOM.

257   **3. Data processing with a strong wind event**

258   **3.1 Basic information of WISSDOM synthesis**

259   A small domain near the northeastern coast of South Korea was selected to derive detailed

260   3D winds over complex terrain (in the black box in the inset map in Fig. 1) because relatively

261   dense and high-quality wind observations were only collected in this region during ICE-POP

262   2018. The size of the WISSDOM synthesis domain is 12×12 km^2 (up to 3 km MSL height) in

263   the horizontal (vertical) direction with 50 m grid spacing. Such high spatial resolution 3D winds

264   were synthesized every 1 hour in this test. Note that the output time steps are adjustable to be

265   finer (recommended limitation is 10 mins), but they are highly related to the temporal resolution

266   of various datasets and computing resources. Two scanning Doppler lidars are located near the

267   center of the domain: one is the equipped "WINDEX-2000" (the model's name from the

268   manufacturer) at the May Hills Supersite (MHS) site, and the other is the "Stream line-XR" at

269   the DaeGwallyeong regional Weather office (DGW) site. In addition to the operational AWS

270   (727 stations), additional surface observations (32 stations) are also involved in ICE-POP 2018

271   surrounding the MHS and DGW sites and the venues of the winter Olympic Games. The

272   soundings are launched at the DGW site every 3 hours during the research period. The LDAPS

273   also provided high spatial resolution of wind information in the test domain. The horizontal

274   distribution of all instruments and datasets used are shown in Fig. 1.
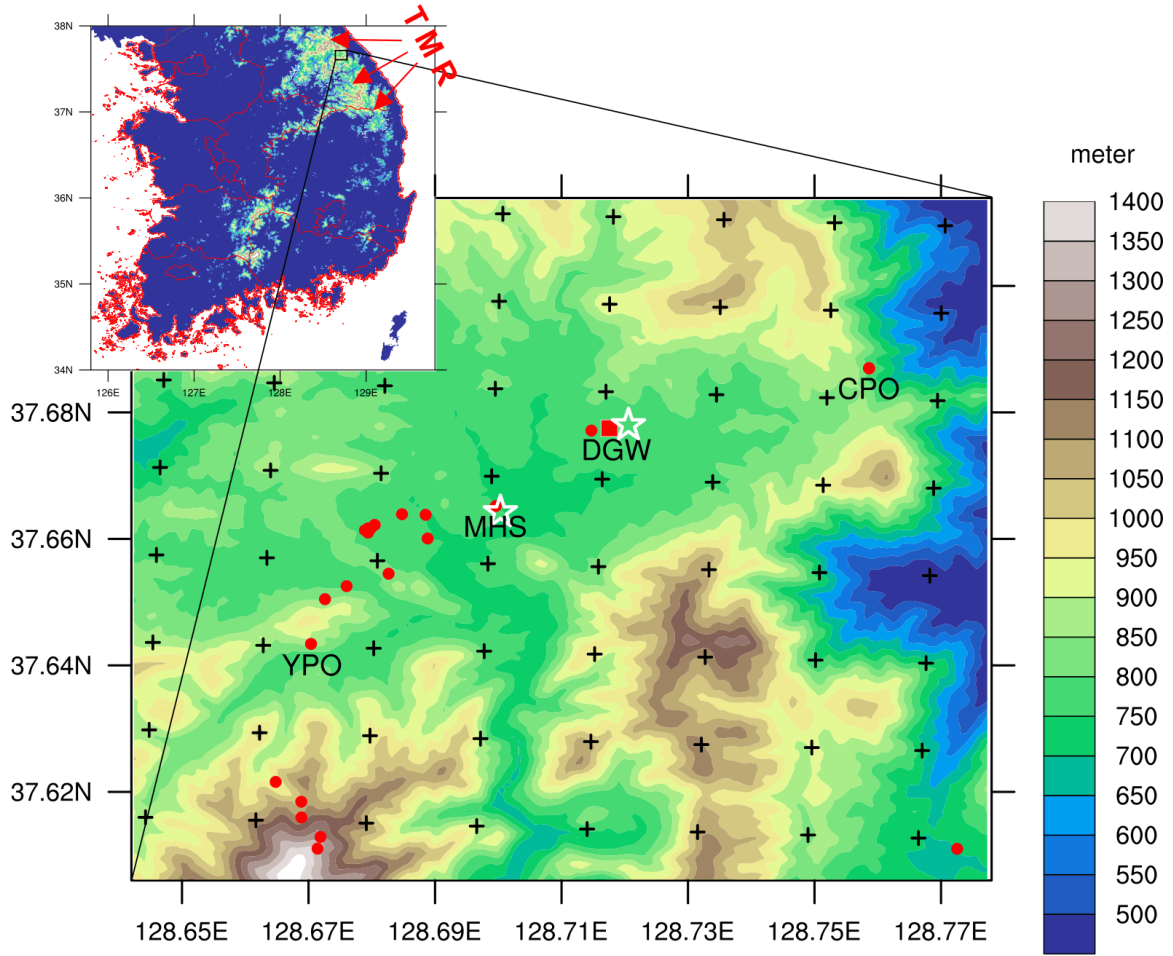
Figure 1. Horizontal distribution of instruments and datasets used in this study. A small box in the upper map indicates the WISSDOM synthesis domain. The Doppler lidars are marked by start symbols at the MHS and DGW sites. Red solid circles and square indicate the automatic weather station (AWS) and sounding, respectively. The black cross marks the data points of LDAPS. Topographic features and elevations are shown with the color shading in a color bar in the figure. The location of the Teabeak Mountain Range (TMR) is also marked.

3.2 Data implemented in WISSDOM synthesis

3.2.1 Scanning Doppler lidars

The radial velocity observed from two scanning Doppler lidars was utilized to retrieve 3D winds via WISSDOM synthesis. The original coordinate system of observed lidar data is not a Cartesian coordinate system, but a spherical (or polar) coordinate system as a plan position indicator (PPI) and hemispheric range height indicator (HRHI) or the RHI. Although relatively dense and complete coverage of wind information (i.e., radial velocity of aerosols) were

288   sufficiently recorded by lidar observations, the collected data are usually not located directly on

289   the given grid points in the WISSDOM synthesis (i.e., Cartesian coordinate system). In this study,

290   the lidar data were interpreted simply from the lidar coordinate system to the Cartesian coordinate

291   system via bilinear interpolation.

292   The scanning strategy of the lidar at the DGW site includes five elevation angles for PPI (7°,

293   15°, 30°, 45°, and 80° before 10:00 UTC on 14 Feb. 2018 and 4°, 8°, 14°, 25°, and 80° after 10:00

294   UTC) and two HRHIs at azimuth angles of 51° and 330°. A full volume scan included all PPIs

295   and HRHIs every ~12 min. The maximum observed radius distance is ~13 km, and the grid

296   spacing is 40 m for each gate along the lidar beam. The scanning strategy of the lidar at the MHS

297   site involves seven elevation angles for PPI (5°, 7°, 10°, 15°, 30°, 45°, and 80°) and one HRHI

298   at an azimuth angle of 0°. A full volume scan included all PPIs and RHIs every ~12 min. The

299   maximum observed radius distance was ~8 km, and the grid spacing was 60 m. The vertical

300   distribution of lidar data in the test domain is shown as blue lines in Fig. 2a.

301   **3.2.2 Automatic weather station (AWS)**

302   Most of the AWS ~~stations~~ are not exactly located on the given grid points of the Cartesian

303   coordinate system. Objective analysis (Cressman, 1959) is a popular way to correct semirandom

304   and inhomogeneous meteorological fields into regular grid points. ~~Not~~Notably,~~e~~ that the wind

305   directions and ~~wind~~ speed must be the first project with the values along the u- and v-components,

306   and then,   ~~interpolate~~ their values must be interpolated individually to the given grids. This study

307   adopted objective analysis for the AWS observations with adjustable RI distances between 100

308   m and 2000 m. After this first step, the observational data can reasonably interpolate to the given

309   grid points horizontally. Furthermore, an additional step is required to put these interpolated data

310   into the given grid points at different vertical levels because the AWS are located at different

311   elevations in the test domain. In the traditional way of original WISSDOM, the interpolated data

312   are moved to the closest level with the shortest distance just above the AWS site. However, the

313 interpolated data are NOT moved to the closest level if the shortest distances are large like more

314 than half (50%) of grid spacing. Nevertheless, to include more data from the AWS observations

315 appropriately, adjusted distances between the AWS sites and given grid points at different vertical

316 levels were necessarily considered. These adjusted distances can be named as vertical extension

317 (VE) here, and there are two options of 50% and 90% in the tests of this study, which correspond

318 to 25 m and 45 m extensions between each grid (in case of the grid spacing is 50 m), respectively.

319 An example demonstrated how to implement the interpolated data to the given grid points by

320 adjustable VE after step one (Fig. 2b).

321   In Fig. 2b, the interpolated data do not need to move to a given grid point (as an example, at

322 the 800 m level here) if the elevation of the AWS is equal to the height of a given grid point as

323 point A. When the AWS is located higher than a given grid point (as point B in Fig. 2b) and does

324 not reach the lower boundary of VE (50%) from the upper given grid point (i.e., at the 850 m

325 level), this interpolated data will be removed and wasted. In contrast, when the interpolated data

326 are located just below the given grid point with 50% VE, it will be achieved in the WISSDOM

327 synthesis at the 800 m level (point C in Fig. 2b). The interpolated data of point D have a similar

328 situation to point B; however, it will be achieved at the 800 m level because a higher VE (90%)

329 was applied here. Since the locations of the AWS are semirandom with relatively sparse or

330 concentrated distributions, the optimal RI and adjustable VE make it possible to include more

331 AWS observations in the WISSDOM synthesis.
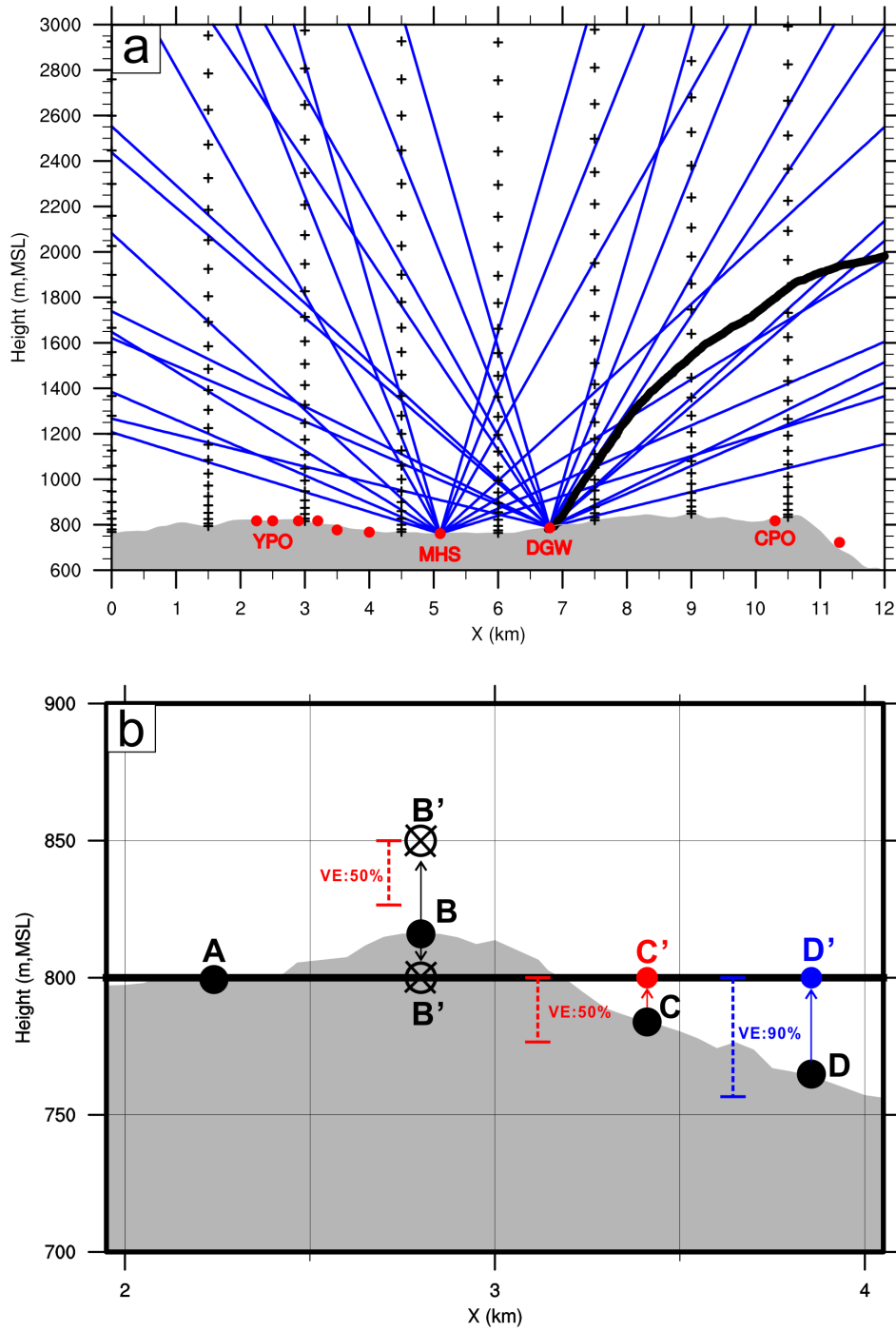
Figure 2. (a) Schematic diagram of the vertical distribution of adopted lidar datasets. Blue lines indicate the lidar data observed at the DGW and MHS sites with different elevation angles. The AWS ~~stations~~ are located on the ground and are marked by solid red circles. An example of a sounding track launched from the DGW site in one time step (06:00 UTC on 14 Feb. 2018) is plotted as a thick black line. The black cross marks indicate the vertical distribution of the LDAPS dataset. (b) Schematic diagram for data implementation with various locations of the AWS ~~stations~~ and different percentages of VE (vertical extension) from given grid points at the 800 m MSL level (thick black line). The gray shading on the bottom represents the topography.

3.2.3 Sounding

341   During ICE-POP 2018, the soundings are launched at the DGW site every 3 hours (from

342   00Z). Vertical profiles of air pressure, temperature, humidity, wind speed and directions were

343   recorded every second (i.e., ~3 m vertical spatial resolution) associated with the rising sensor.

344   The sounding sensor drifted when rising, and an example of its track in one time step is shown

345   as a thick black line in Fig. 2a. In this example, the sounding movement was mostly affected by

346   westerly winds, and it measured the meteorological parameters in any location along the track in

347   the test domain. The coordinate system of sounding data is quite similar to the distribution of

348   AWS measurements, and the observations are not located right on the given grid points of the

349   WISSDOM synthesis.

350   Similar to the AWS data, the sounding data also underwent objective analysis with an

351   adjustable RI distance for the wind measurements in the first step. Then, the interpolated data

352   were switched to given grid points for each vertical level by the different VE in the WISSDOM

353   synthesis.

354   **3.2.4 Reanalysis dataset: LDAPS**

355   The local reanalysis dataset LDAPS was generated by the KMA. This dataset provides u-

356   and v-component winds every 3 hours, and the horizontal spatial resolution is ~1.5 km with the

357   grid type in Lambert Conformal (as black cross marks in Fig. 1). The data revealed denser

358   distributions near the surface and sparse distributions at higher levels (see Fig. 2a). The initiations

359   of wind variables in the LDAPS were assimilated with many observational platforms, including

360   radar, AWS, satellite and sounding data. Thus, the relatively high reliability of this dataset could

361   be expected. In addition, such datasets have also significantly improved the forecast ability in

362   small-scale weather phenomena over complex terrain in Korea (Kim et al., 2019, Choi et al.,

363   2020, Kim et al., 2020).

364   The LDAPS data are not located directly on the given grid points of the WISSDOM synthesis

365   system. Unlike the distribution of AWS and sounding observations, LDAPS has dense and good

366   coverage in the test domain. The Cartesian coordinate is the most efficient ~~way~~ method and the

367   best system for partial differential equations (Armijo, 1969), and ~~then~~ it is also ~~be~~ used in the cost

368   function of WISSDOM (Liou and Chang, 2009). In this study, the horizontal and vertical

369   resolutions of given grid points were primarily determined by the characteristics of lidar data.

370   Therefore, ~~like~~ similar to lidar observations, the LDAPS data were also interpolated to the given

371   grid points on the Cartesian coordinate system via the bilinear interpolation method.

3.3 Overview of the selected strong wind event

373   A strong wind event was selected to evaluate the performance of this modified WISSDOM

374   synthesis scheme. In this strong wind event, the evolution of surface wind patterns on the Korean

375   Peninsula was mainly dominated by a moving LPS which is one type of strong downslope winds

376   (Park et al, 2022, Tsai et al., 2022). The LPS moved out from China and penetrated the northern

377   part of the Korean Peninsula through the Yellow Sea beginning at approximately 12:00 UTC on

378   13 February 2018. Consequently, a relatively strong surface wind speed (exceeding ~17 m s^{-1})

379   was observed when the LPS was located near the northeastern coast of the Korean Peninsula

380   (~130°E, 40°N) at 00:00 UTC on 14 February 2018 (Fig. 3). Then, the surface wind speed became

381   weak when the LPS moved away from South Korea after 00:00 UTC on 15 February 2018 (not

382   shown); the details of the synoptic conditions can be found in Tsai et al. (2022).

383
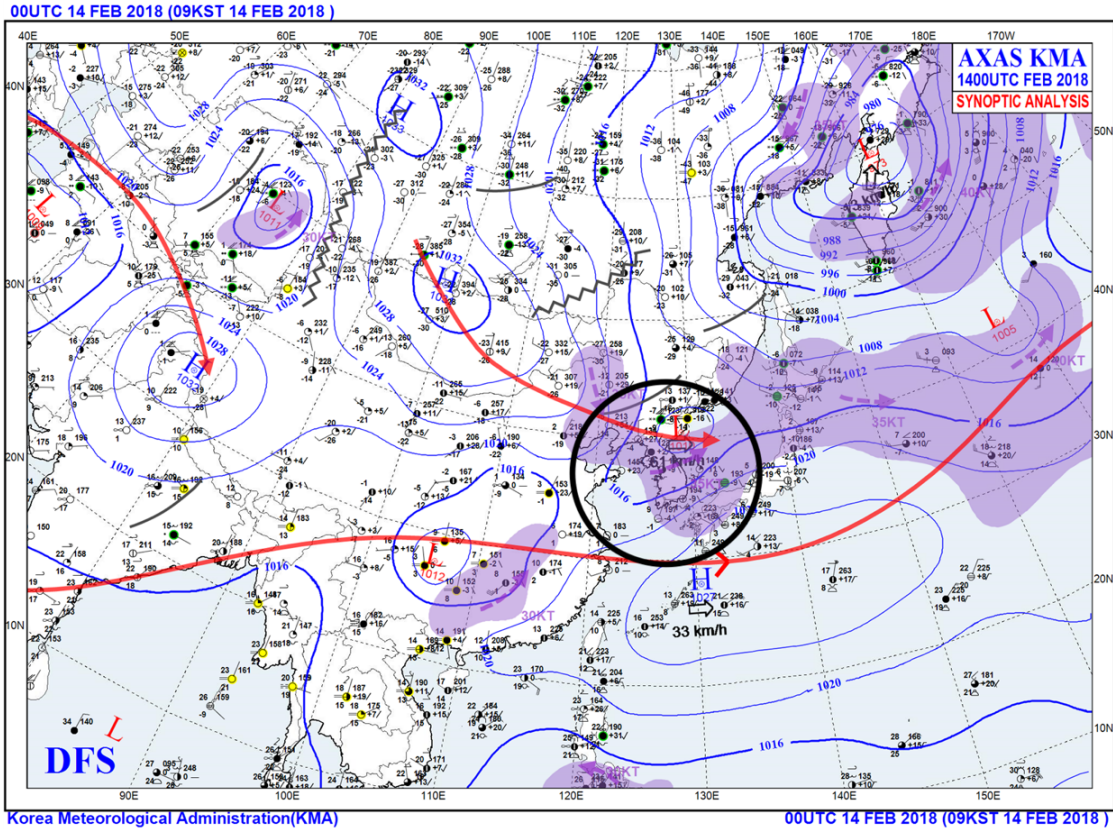
384 Figure 3. Synoptic surface chart from the Korea Meteorological Administration (KMA) at 00:00 UTC on 14 Feb.

385   2018. The locations of the Korean peninsula and the LPS has been marked by black circle.

386

387   This event is one of two strong wind events (i.e., daily maximum wind speeds larger than

388 10 m s^{-1} observed at the AWS sites along the northeastern coast of South Korea) in the past

389 decade based on the KMA historic record. Such a strong wind event may help us to examine the

390 potential maximum errors of the retrieved winds. Since persistent, strong westerly winds were

391 observed by the soundings and AWS from near the surface and upper layers over the TMR during

392 the event, the data coverages in the test domain were checked during a chosen time step (06:00

393 UTC on 14 February 2018). The percentage of data occupations for each dataset (after

394 interpolation) was checked, and the results are shown in Fig. 4. Note that the elevation of the

395 TMR is approximately 700 m MSL in the test domain. The lidars provided good coverage of

396 100% to 50% at the lower layers between 700 m and 800 m MSL. The coverage of lidars was

397 reduced significantly above 900 m MSL and remained at ~5% due to the scan strategy during the

398 Olympic games (more dense observations near the surface). The maximum coverage of the AWS

399   observations is ~40% at 800 m, and there was less coverage above this layer since relatively few

400   AWS ~~stations~~ are located in the higher mountains. Because only one sounding observation was

401   utilized in this domain, relatively few coverages were also depicted. The local reanalysis LDAPS

402   can provide complete coverage above 900 m MSL (exceeding 100%), albeit there was less

403   coverage in the lower layers due to terrain. The lidar, sounding, and AWS observations covered

404   most areas at lower levels but not higher levels; thus, the LDAPS compensated for most of the

405   wind information at the upper layers in the WISSDOM synthesis.

406
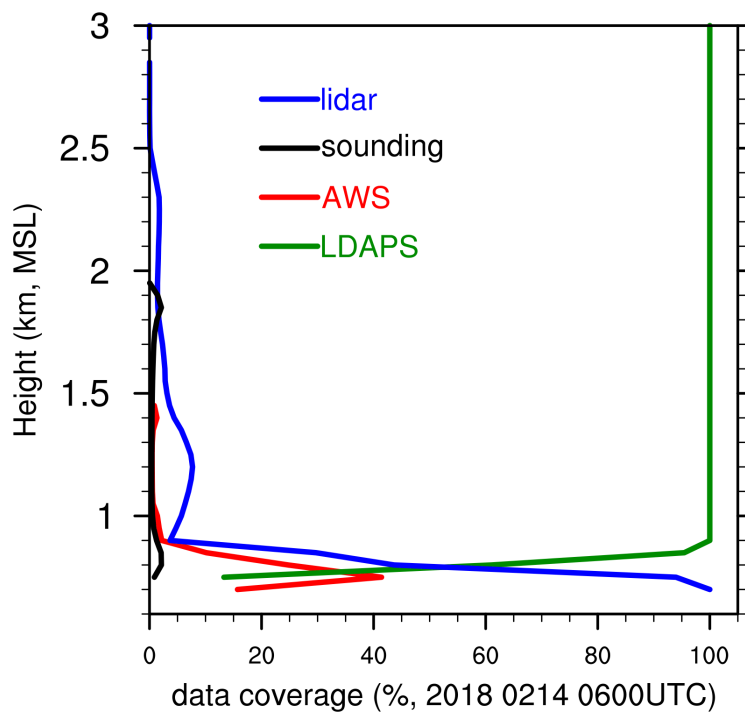
407   Figure 4. Data coverage (percentage, %) of the lidar (blue line), sounding (black line), AWS (red line) observations,

408   and LDAPS (green line) at 06:00 UTC on 14 Feb. 2018.

409   **4. Control run and the accuracy of WISSDOM**

410   **4.1 Control run**

411   Relatively reliable 3D winds were derived by a control run of the WISSDOM synthesis

412   because all available wind observations and local reanalysis datasets were appropriately acquired.

413   These datasets provided sufficient and complete wind information with a high percentage of

coverage in the test domain (cf. Fig. 4). Therefore, the retrieved winds from the control run can be treated as the optimal results (i.e., analytic expression of variational-based scheme) in WISSDOM. The control run was performed carefully with the necessary procedures in data implementation before running the WISSDOM synthesis as follows. The lidar and LDAPS datasets must perform bilinear interpolation to the given grid points in WISSDOM, and the sounding and AWS observations must undergo objective analysis with the appropriate RI distance and VE. The quantities of the weighting coefficients for each input dataset followed the default setting from the original version of WISSDOM. The 3D winds were derived during one time step at 06:00 UTC on 14 Feb. 2018 and compared with conventional observations. Note that the best weighting weights havecoefficients have been determined by a series of observation system simulation experiment (OSSE) type tests from Liou and Chang (2009)., Tthey have putted more weighting coefficientss in observations and less fewer weights in modeling inputs. Based on the experiences and the default setting of weighting coefficients weights from previous their studies, the basic setting of the control run has beenwas first decided. Consequently, sensitivity tests were performed to better understand the possible variances associated with different weighting coefficients when the lidar data were implemented. The basic setting of this control run is summarized in Table 1.

Table 1 Basic setting of WISSDOM (control run)

Domain Range	Latitude: 37.606°N~37.713°N Longitude: 128.642°E~128.778°E
Domain Size	12 × 12 × 3 km (long × width × vertical)
Spatial Resolution	0.05 × 0.05 × 0.05 km (long × width × vertical)
Terrain Resolution	0.09 km
Coordinate System	Cartesian coordinate system
Background	Sounding (DGW)
Data Implementation	Doppler Lidars (MHS, DGW): bilinear interpolation AWS: objective analysis (RI*: 1 km, VE*: 90%) Sounding (DGW): objective analysis (RI: 1 km, VE: 90%)

	LDAPS: bilinear interpolation
Weighting Coefficient (input datasets)	Doppler Lidars (α_1): 10^6 Background (α_2): 10^2 Sounding (α_6): 10^6 AWS (α_7): 10^6 LDAPS (α_8): 10^3

*RI: radius influence, VE: vertical extension

431   The results of 3D winds at 800 m MSL derived from the control run are shown in Figs. 5a,

432   c, and e. Topographic features comprised relatively lower elevations in the center of the test

433   domain, and there were weaker u-component winds (~7 m s^{-1}) near the AWS and MHS lidar sites

434   between 128.67°E and 128.71°E (Fig. 5a). In contrast, the u-component winds (~15 m s^{-1}) were

435   almost doubled near the DGW lidar site (between 128.71°E and 128.73°E). The vertical

436   structures of the u-component winds across these two lidars (i.e., along the black line in Fig. 5a)

437   are shown in Fig. 5b. The strength of the u-component winds rapidly increased from the surface

438   to the upper layers (from ~6 to 20 m s^{-1}), and uniform u-component winds with wavy pattern

439   were depicted above ~1 km MSL except for the stronger winds near the surface surrounding the

440   DGW site. There were relatively weak (strong) u-component winds surrounding the lidar at the

441   MHS (DGW) site near the surface. Relatively weak v-component winds were found

442   (approximately ±4 m s^{-1}) at 800 m MSL (Fig. 5c); thus, the horizontal wind directions were

443   mostly westerly winds during this time step. The v-component winds were obviously accelerated

444   in several local areas encompassing the terrain (near 128.71°E). The vertical structure of the v-

445   component winds (Fig. 5d) indicates that the v-component winds became stronger in the upper

446   layer. The wind directions were changed from westerly to southwesterly from the near surface

447   up to ~1.4 km MSL height. Updrafts were triggered on windward slopes when westerly winds

448   impinge the terrain or hills (Figs. 5e and 5f). Basically, the 3D winds derived from the WISSDOM

449   synthesis reveal reasonable patterns compared to synoptic environmental conditions (cf. Fig. 3);

450   the moving LPS accompanied stronger westerly winds.

451
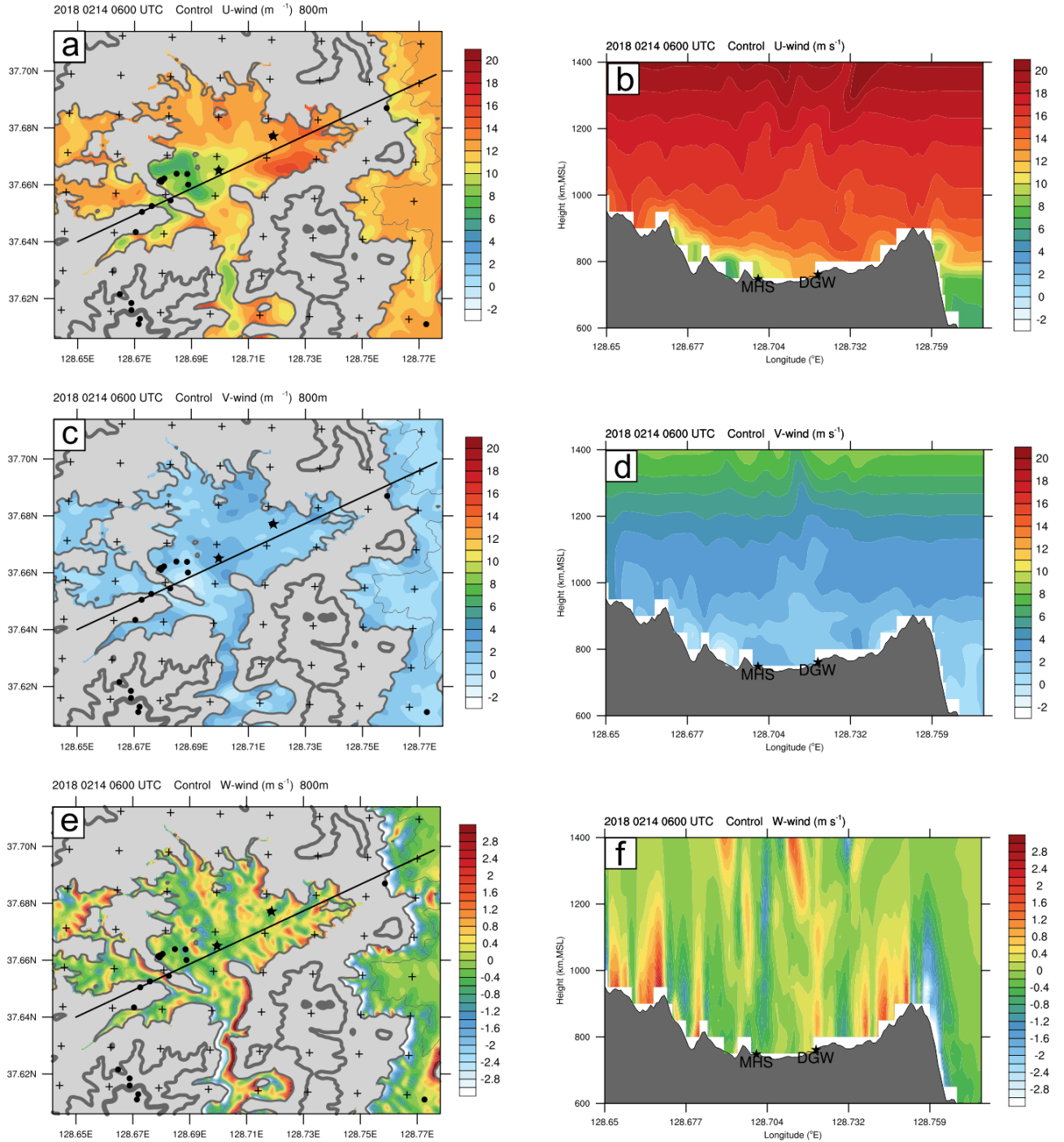
452 Figure 5. The 3D winds were derived from the control run by the WISSDOM synthesis at 06:00 UTC on 14 Feb.

453   2018. (a) The u-component winds (color, m s⁻¹) at 800 m MSL; the gray shading represents the terrain area, and

454   the contours indicate different terrain heights of 600 m, 800 m and 1000 m MSL corresponding to thin to thick

455   contours. The locations of lidars are marked with asterisks. (b) Vertical structures of u-component winds (color,

456   m s⁻¹) along the black line in (a) The gray shading in the lower part of the figure indicates the height of the terrain.

457   (c) and (d) are the same as (a) and (b) but for the v-component winds. (e) and (f) are the same as (a) and (b) but

458   for the w-component winds.

4.2 Intercomparison between derived winds and observations

Detailed analyses were performed in this section to quantitatively evaluate the accuracy of the optimally derived 3D winds from the WISSDOM synthesis. Two kinds of instruments were available in the test domain to detect the relatively realistic winds: sounding and lidar quasi-vertical profiles (QVP, Ryzhkov et al., 2016), a profile of QVP can be general form a lidar. The QVP of horizontal and vertical winds were retrieved based on the so-called velocity-azimuth display (VAD) technique (Browning and Wexler, 1968, Gao et al., 2004). We regressed the Fourier coefficients of the Doppler velocities of the 80° PPI under the linear horizontal wind assumption and obtained the horizontal wind profile. The vertical (i.e., w-component) wind was retrieved under the assumptions of constant vertical wind, zero terminal velocity of aerosol particles, and no horizontal divergence [see Kim et al. (2022) for details on the wind retrieval]. The accuracy of the retrieved wind profile is suitable for the WISSDOM wind evaluation, given the low root mean square deviation (RMSD) of < 2.5 m s^{-1} and high correlation coefficient of > 0.94 of horizontal wind speed as shown in the comparison against 487 rawinsondes (Kim et al., 2022). The horizontal winds observed from the soundings and the 3D u-, v-, and w-component winds of the lidar QVP at the DGW site were utilized to represent the observations.

A complete analysis of the intercomparison between the WISSDOM synthesis and observations is presented in the following subsections. Because the verification observations are being used in the WISSDOM synthesis, the results of the control run are not verified independently; nevertheless, detailed discussions regarding the results of the sensitivity tests for the observations are presented in Section 5.

4.2.1 Sounding

The discrepancies in horizontal winds derived from WISSDOM and the sounding observations for the entire research period (from 12:00 UTC on 13 to 12:00 UTC on 14 February

483   2018) were analyzed. Fig. 6 shows the scatter plots of the u- and v-component winds on the

484   locations following the tracks of sounding launched from the DGW site. Most of the u-component

485   winds derived from WISSDOM are in good agreement with the sounding observations, and the

486   wind speed is increased with the height from approximately 10 to 40 m s⁻¹. Slight underestimation

487   of retrieved u-component winds can be found at the layers of 1.5~2 km MSL (Fig. 6a). In contrast,

488   most of the v-component winds were weak (smaller than 15 m s⁻¹) at all layers, because the

489   environmental winds were more like westerlies during the research period. There were also

490   slightly overestimated v-component winds derived from WISSDOM at the layers of 1.5~2 km

491   MSL (Fig. 6b). The possible reason why the overestimated winds occurred above ~1.5 km MSL

492   is that lidar data had relatively less coverages at higher layers (cf. Fig. 4).

493
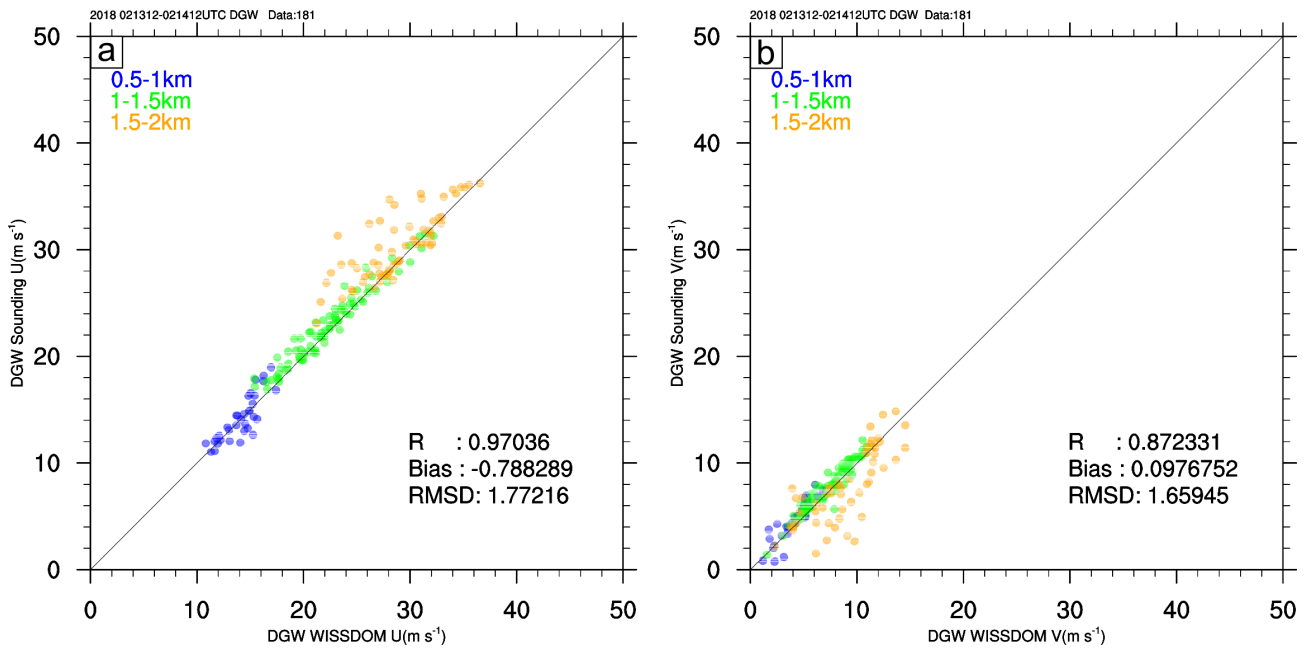
494   Figure. 6. Scatter plots of (a) u-component winds between the WISSDOM synthesis (x-axis) and sounding

495   observations (y-axis) above the DGW site during the research period. The colors indicate different layers, and

496   the numbers of data points, correlation coefficients, average biases and root mean square deviations are also

497   shown in the figure. (b) The same as (a) but for v-component winds.

498   Overall, the u-component winds show a high correlation coefficient (exceeding 0.97), low

499   average bias (−0.78 m s⁻¹), and the root mean square deviation (RMSD) of 1.77 m s⁻¹. The

500   correlation coefficient of the v-component is also high (0.87), the average bias is 0.09 m s⁻¹, and

501   the RMSD is 1.65 m s⁻¹.
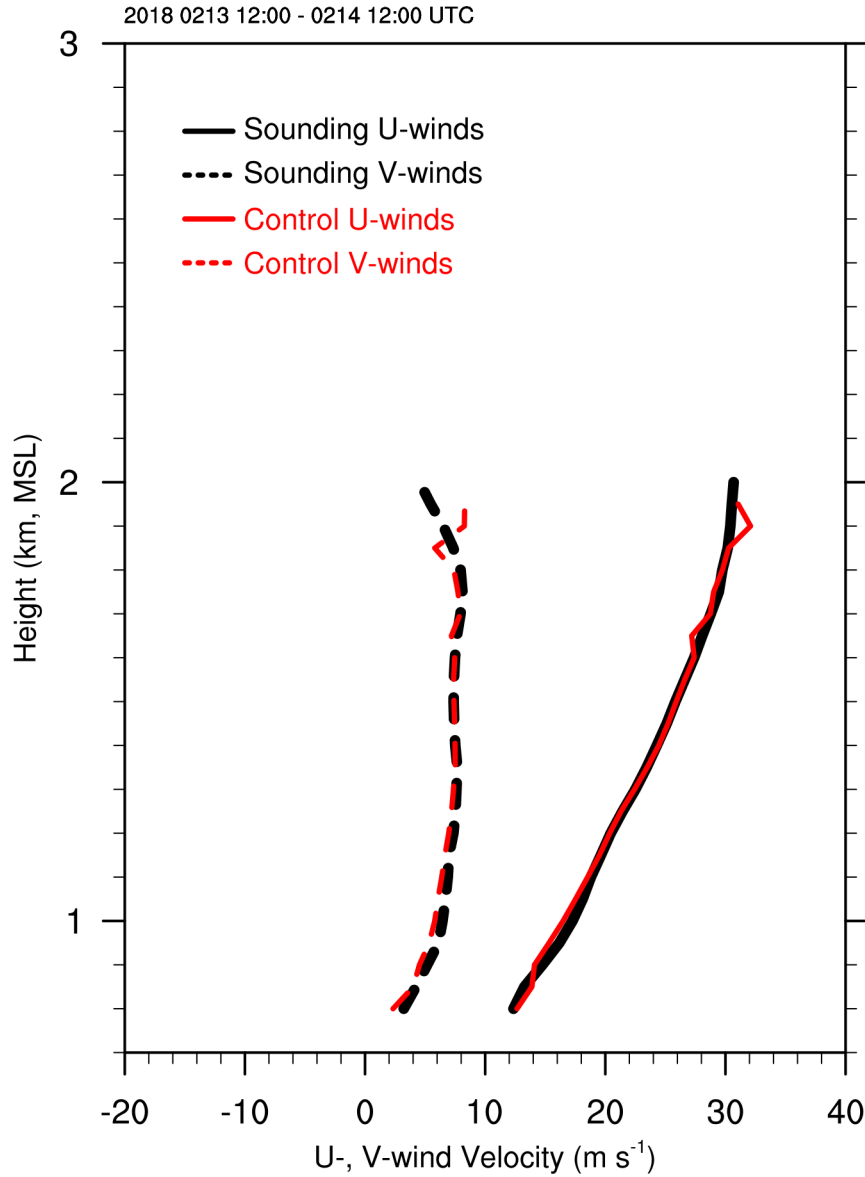
Figure 7. Vertical wind profiles of average horizontal winds derived from the WISSDOM synthesis (red lines and vectors) and sounding observations (black lines and vectors) above the DGW site from 12:00 UTC on 13 to 12:00 UTC on 14 Feb. 2018. Solid lines indicate u-component winds (m s⁻¹), and dashed lines indicate v-component winds (m s⁻¹).

The vertical profiles of the averaged u- and v-component winds for the period of 12:00 UTC on 13 to 12:00 UTC on 14 Feb. 2018 is shown in Fig. 7 for the WISSDOM synthesis (red) and sounding observations (black) launched from the DGW site. The average profiles agree well except for the height above 1.5 km MSL, slight discrepancies of u- and v-component winds (< 1 m s⁻¹). Their statistical errors during the entire research period were quantified by the box plot

512 shown in Fig. 8.

513   The maximum difference in wind directions between the WISSDOM synthesis and sounding

514 observations is small at all layers. ~~Except for~~Only relatively larger IQR ~~existed~~ (between ~−5 and

515 5 degrees) and larger median values (between ~0 and 5 ~~degrees~~) can be found at the lowest level~~.~~,

516 Tthe interquartile range (IQR) and median values of the wind direction differences are smaller

517 (between ~0 and 2.5 degrees) during the entire research period (Fig. 8a). Basically, the IQR and

518 median values of the wind direction differences are close to 0 degrees above 1 km MSL. Fig. 8b

519 shows the difference in wind speed between the WISSDOM synthesis and sounding observations.

520 The differences of wind speed derived from WISSDOM was slightly underestimated in the layers

521 between ~0.85 and 1.3 km MSL. The median values of the wind speed differences were between

522 −1 and 0.5 m s^{-1}, and the IQR of wind speed differences was between −2 and 0.5 m s^{-1}. Above

523 1.3 km MSL, the differences in wind speed are small as their median values are close to 0 m s^{-1}.

524

525
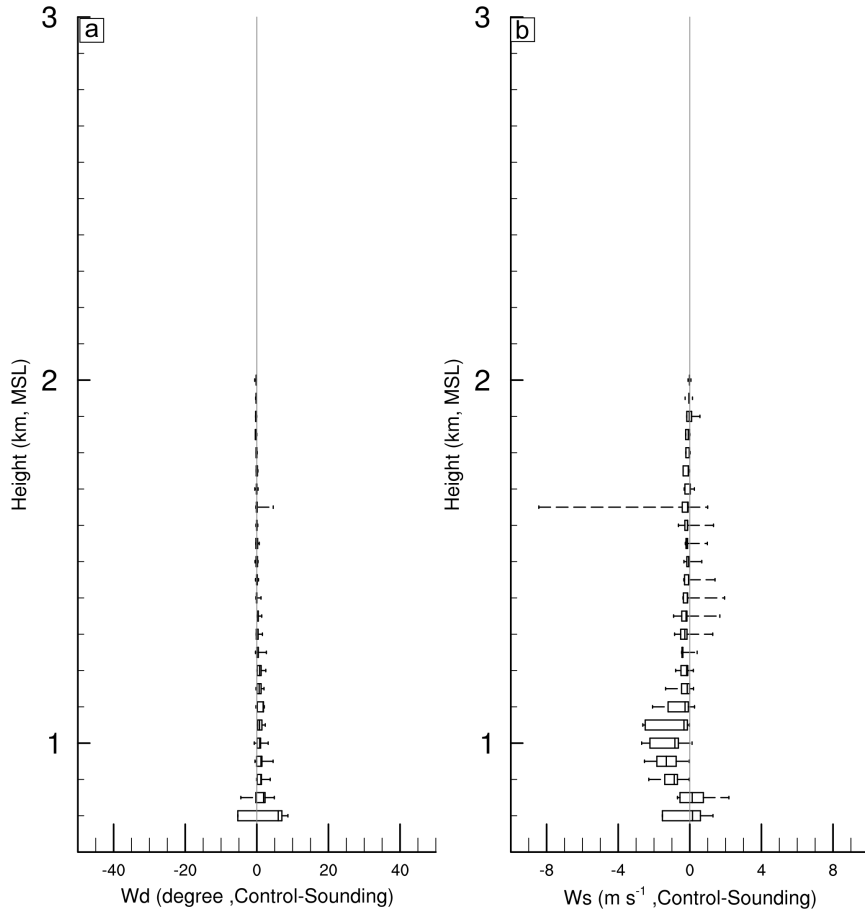
526 Figure 8. The box plot of average (a) wind direction discrepancies between the WISSDOM synthesis and sounding
527   observations above the DGW site during the research period. (b) Same as (a) but for the wind speed.

4.2.3 Lidar QVP

529   The lidar QVP is another observational reference used to evaluate the performance of derived

530 winds from the WISSDOM synthesis. The scatter plots of the horizontal winds derived from

531 WISSDOM and lidar QVP at the DGW site are shown in Fig. 9. The strength of the u-component

532 winds increases with height in the range between approximately 10 m s^{-1} and 40 m s^{-1} from the

533 surface up to ~2.5 km MSL (Fig. 9a). Although the results show a relatively high correlation

534 coefficient (0.84) for the u-component winds from lower to higher layers in the entire research

535 period, the degree of scatter is larger than that in Fig. 6a. The average bias and RMSD of the u-

536 component winds are 2.83 m s^{-1} and 3.69 m s^{-1}, respectively. The correlation coefficient of v-

537 component winds is lower (0.35) in association with low wind speed (<15 m s^{-1}) from the surface

538 to 2.5 km MSL (Fig. 9b), and it may possibly relate to less coverages from lidar QVP data at

539 higher layers. The average bias and RMSD of the v-component winds are 2.26 m s^{-1} and 2.92 m

540 s^{-1}, respectively. The results of these scatter plot analyses are summarized in Table 2. Basically,

541 the u-component winds have high correlations, relatively lower bias, and lower RMSD than the

542 v-component winds because the environmental winds are more westerly.

543
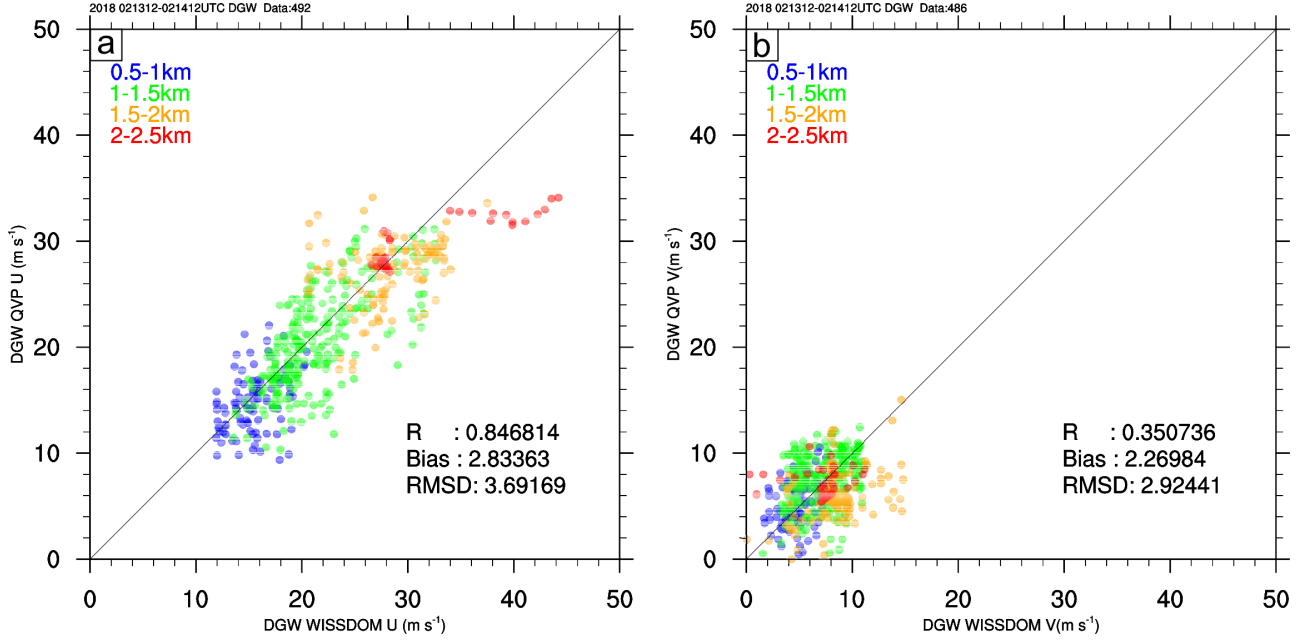
544 Figure 9. The same as Fig. 6 but for (a) u-component winds between the WISSDOM synthesis (x-axis) and lidar

545   QVP (y-axis). (b) The same as (a) but for v-component winds.

546

Table 2  Summary of the intercomparisons between WISSDOM and observations

		Correlation coefficient	Average bias (m s^{-1})	RMSD (m s^{-1})
WISSDOM-sounding	u-component	0.97	-0.78	1.77
	v-component	0.87	0.09	1.65
WISSDOM-lidar QVP	u-component	0.84	2.83	3.69
	v-component	0.35	2.26	2.92

547    Compared to the sounding observations, additional w-component winds are available in

548 lidar QVP, which allows us to check their discrepancies in 3D winds. However, most of the

549 vertical velocity observations were quite weak (approximately ±0.2 m s^{-1}) above the DGW site,

550 and relatively low reliability of the derived vertical velocity could be expected in this event.

551 Therefore, the average vertical profiles of 3D winds were utilized to qualitatively check the

552 discrepancies between WISSDOM synthesis and lidar QVP during the research period (Fig. 10).

553 The results show that the average u-component winds have relatively smaller discrepancies

554 (approximately <1 m s^{-1}) between the WISSDOM synthesis (marked as WISS-U in Fig. 10) and

555 lidar QVP (marked as QVP-U) below ~1.3 km MSL at the DGW site. In contrast, there were

556 larger discrepancies (approximately >2 m s^{-1}) between 1.3 km and 2 km MSL. The average v-

557   component winds derived from WISSDOM (marked as WISS-V) and lidar QVP (QVP-V) were

558   generally weak, and the ranges of WISS-V and QVP-V were between ~2 m s^{-1} and 8 m s^{-1}.

559   Generally, the vertical profiles of WISS-V were nearly overlain with QVP-V, and their

560   discrepancies existed in the height range 1.6~2.0 km MSL (maximum ~4 m s^{-1}). Smaller (larger)

561   discrepancies of w-component winds were significantly below (above) the height at ~1.3 km

562   MSL (maximum discrepancies ~0.6 m s^{-1} at 1.7 km MSL). Despite the larger discrepancies, the

563   similar patterns of W can also be shown. In summary, the discrepancies in the 3D winds between

564   the WISSDOM synthesis and lidar QVP were small in the lower layers and large in the higher

565   layers because the observational data from lidars and AWS provided good quality and sufficient

566   wind information at the lower layers but not in the higher layers (lower coverages of lidar data

567   above 1.3 km MSL, cf. Fig. 4).

568
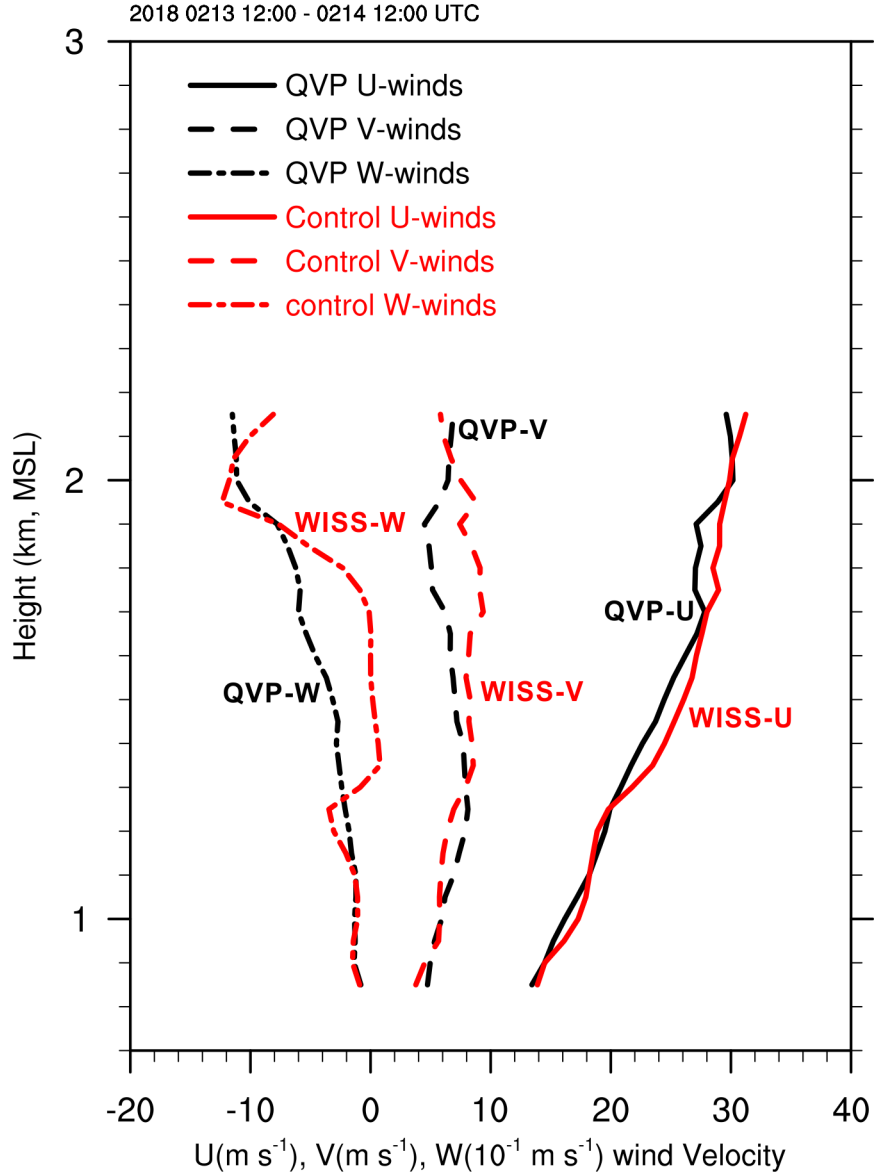
569 Figure 10. Vertical wind profiles of average 3D winds derived from the WISSDOM synthesis (red lines and vectors)

570   and lidar QVP (black lines and vectors) above the DGW site from 12:00 UTC on 13 to 12:00 UTC on 14 Feb.

571   2018. Solid lines indicate u-component winds (m s⁻¹), dashed lines indicate v-component winds (m s⁻¹), and

572   dash-dotted lines indicate w-component winds (1×10^1 m s⁻¹). The u-, v-, and w-component winds derived from

573   the WISSDOM synthesis (lidar QVP) were marked by WISS-U (QVP-U), WISS-V (QVP-V), and WISS-W

574   (QVP-W), respectively.

575   Fig. 11 shows the quantile distribution of statistical errors of wind direction, wind speed and

576 vertical velocity between the WISSDOM synthesis and lidar QVP during the research period.

577 The IQR of the wind direction is smaller (−5~5 degrees) in the layers from 0.85 km to 1.5 km

578 MSL and turns to approximately −10~0 degrees above 1.5 km MSL. The median values of wind

579 direction are smaller −5~5 degrees) from near the surface to the upper layers (Fig. 11a). Fig. 11b

580 shows that the median values (IQR) of wind speed are approximately –1~1 m s^{-1} (–2~2 m s^{-1})

581 below 1.5 km MSL, and they all become larger with heights above 1.5 km MSL (between −1 and

582 3 m s^{-1} for median values and −4~4 m s^{-1} for the IQR). The statistical error of the vertical velocity

583 reveals that the IQR is −0.2~0.2 m s^{-1} (−0.8~0.8 m s^{-1}) below (above) 1.3 km MSL, and the

584 median values are 0~0.2 m s^{-1} −0.2~0.6 m s^{-1}) below (above) 1.3 km MSL. The results of

585 statistical errors are summarized in Table 3.

586

587
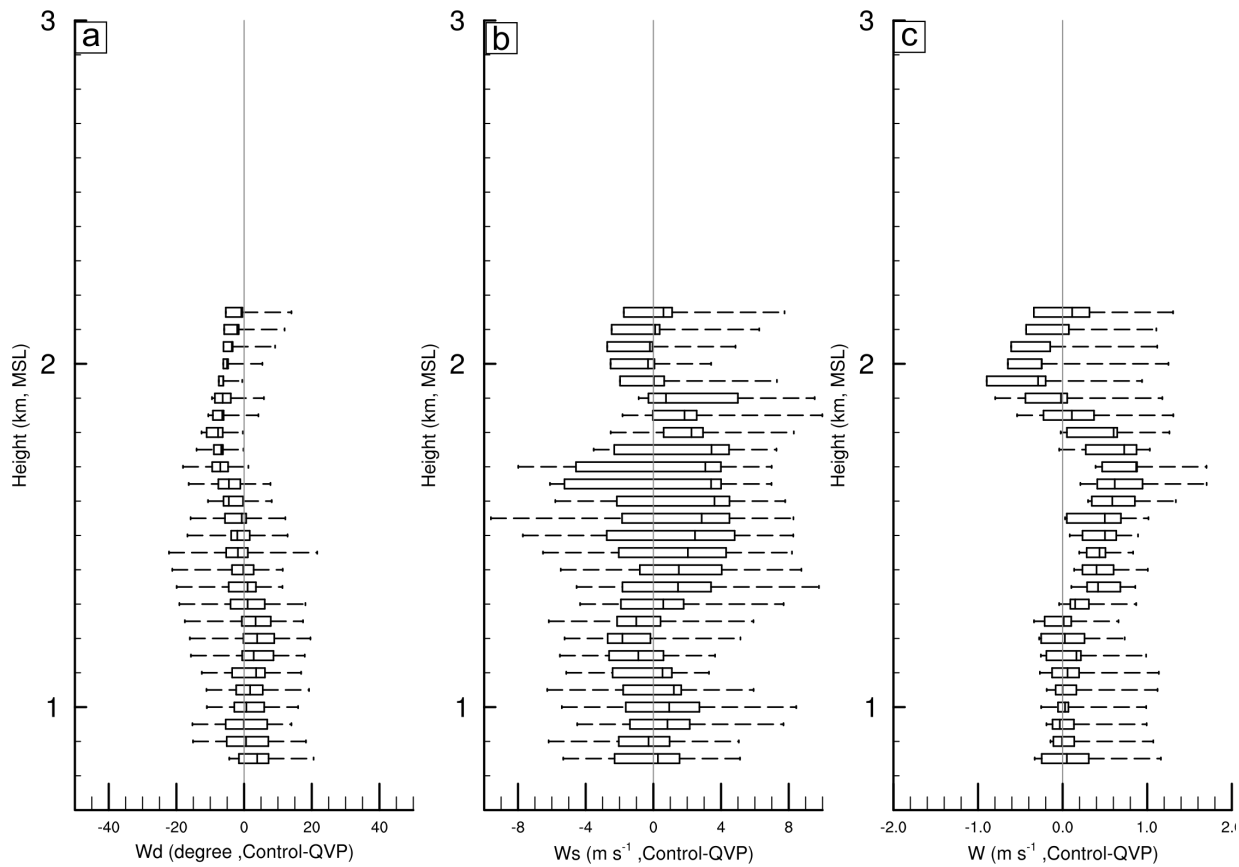
588 Figure 11. The box plot of average (a) wind direction discrepancies between the WISSDOM synthesis and sounding

589 observations above the DGW site during the research period. (b) Same as (a) but for the wind speed. (c) Same

590 as (a) but for the w-component winds.

591

Table 3 Summary of the statistical errors between WISSDOM and observations

		Interquartile range (IQR)	Median values
WISSDOM-sounding	wind direction	0~2.5 (deg.)	0~2.5 (deg.)
	wind speed	−2~0.5 (m s^{-1})	−1~0.5 (m s^{-1})

	wind direction	−10~5 (deg.)	−5~5 (deg.)
WISSDOM-lidar QVP	wind speed	-4~4 (m s^{-1})	−1~3 (m s^{-1})
	w-component winds	−0.8~0.8 (m s^{-1})	−0.2~0.6 (m s^{-1})

5. Sensitivity test with various datasets, data implementation and weighting coefficients

592

5.1 Impacts of various datasets (Experiment A)

593

594   In this ~~session~~section, the impacts of various datasets on data implemented in the WISSDOM

595   synthesis were evaluated. In particular~~,~~, ~~then~~ the quantitative ~~range of errors~~variances ~~can be~~

596   ~~estimated from~~ between each design, control run, sounding observations, and ~~independent~~

597   ~~observation~~the QVP can be estimated. The basic setting of Experiment A took off several inputs

598   from the WISSDOM control run (cf. Table 1) as four designs in Experiment A. The details of

599   these four designs are summarized in Table 4 as the control run without the lidar observations

600   (A-1), the control run without the AWS observations (A-2), the control run without the sounding

601   observations (A-3) and the control run without the LDAPS data (A-4). The discrepancies of 3D

602   winds were examined between the control run and each design in Experiment A. Since the

603   environmental wind speed is nearly comprised of uniform westerlies in this event, the results only

604   show the difference in u-component winds between control run and each design (A-1~A-4) in

605   Fig. 12. An additional test was designed as only Doppler lidar data are used without other

606   constraints from $J_6 \sim J_8$ (A-5) ~~In addition,~~ to evaluate the performances between the modified

607   ~~WISSDOM~~ and original version~~s~~ of WISSDOM. ~~by using Doppler lidar data, additional test was~~

608   ~~designed as only Doppler lidar data are used without additional constraints from $J_6 \sim J_8$ (A-5).~~

609   Fig. 12a reveals the discrepancies in horizontal u-component winds at 800 m MSL as the A-

610   1 is subtracted from the control run. This result reflects the impacts of lidar observations on the

611   u-component winds in the WISSDOM synthesis. The most significant contributions from the

612   lidar observations are the high wind speed existing near the DGW site in a relatively narrow

613   valley. The mechanisms of the accelerated wind speed due to the channeling effect in this local

614   area were verified by our previous study (Tsai et al. 2022). The lidar observations also contributed

615   to the high wind speed in another area near the western side of the MHS site (128.68°E, 37.66°N).

616   Based on the analysis in the vertical cross section of u-component winds in A-1 (Fig. 12b), the

617   lidar observations significantly affected the high wind speed only in the lower levels (below ~900

618   m MSL) but not in the higher levels. Lidar observations provided sufficient coverage only for

619   lower levels and not higher levels (cf. Fig. 4).

620

Table 4 Experiment setting (sensitivity testing)

Control run	Various datasets	Including Doppler lidars, AWS, Soundings, LDAPS
	Interpolation of AWS	RI: 1.0 km, VE: 90%
	Weighting Coefficient	Doppler Lidars (α_1): 10^6 Background (α_2): 10^2 Sounding (α_6): 10^6 AWS (α_7): 10^6 LDAPS (α_8): 10^3
Experiment A	Various datasets	A-1 Excluding Doppler Lidars A-2 Excluding AWS A-3 Excluding Soundings A-4 Excluding LDAPS A-5 Only Doppler lidars
Experiment B	Interpolation of AWS	B-1 RI: 0.5 km, VE: 50% B-2 RI: 0.5 km, VE: 90% B-3 RI: 1.0 km, VE: 50% B-4 RI: 2.0 km, VE: 50% B-5 RI: 2.0 km, VE: 90%
Experiment C	Weighting Coefficient (constraints)	C-1 AWS (α_7): 10^3 C-2 Doppler Lidars (α_1): 10^3 C-3 LDAPS (α_8): 10^6

621

622   The impacts of the AWS cause negative values on the u-component winds in most areas at

623   800 m MSL in A-2 (Fig. 12c), especially in the western areas of the MHS site. Negative

624   contributions of the u-component winds produced by the AWS observations were restricted near

625   the surface, and the low wind speed area was extended to ~100 m above the surface (Fig. 12d).

626   The contributions of the u-component winds from the sounding observations were weak near the

627   DGW sounding site in A-3 (Figs. 12e and 12f). The impacts of u-component winds from the

628   LDAPS datasets were rather smaller in most of analysis area. in A-4 (Figs. 12g and 12h).

629   Relatively weak winds were presented near the surface from the results of A-5 (Figs. 12i and

630   12j), especially at the lower layers. These results reflects that the additional constraints play

631   crucial roles, especially at lower layers. relatively stronger winds were retrieved when additional

632   constraints are removed. Furthermore, it is also implied that the retrieved winds can be reasonably

633   retrieved when additional constraints are setadjusted in the modified version of WISSDOM.

634
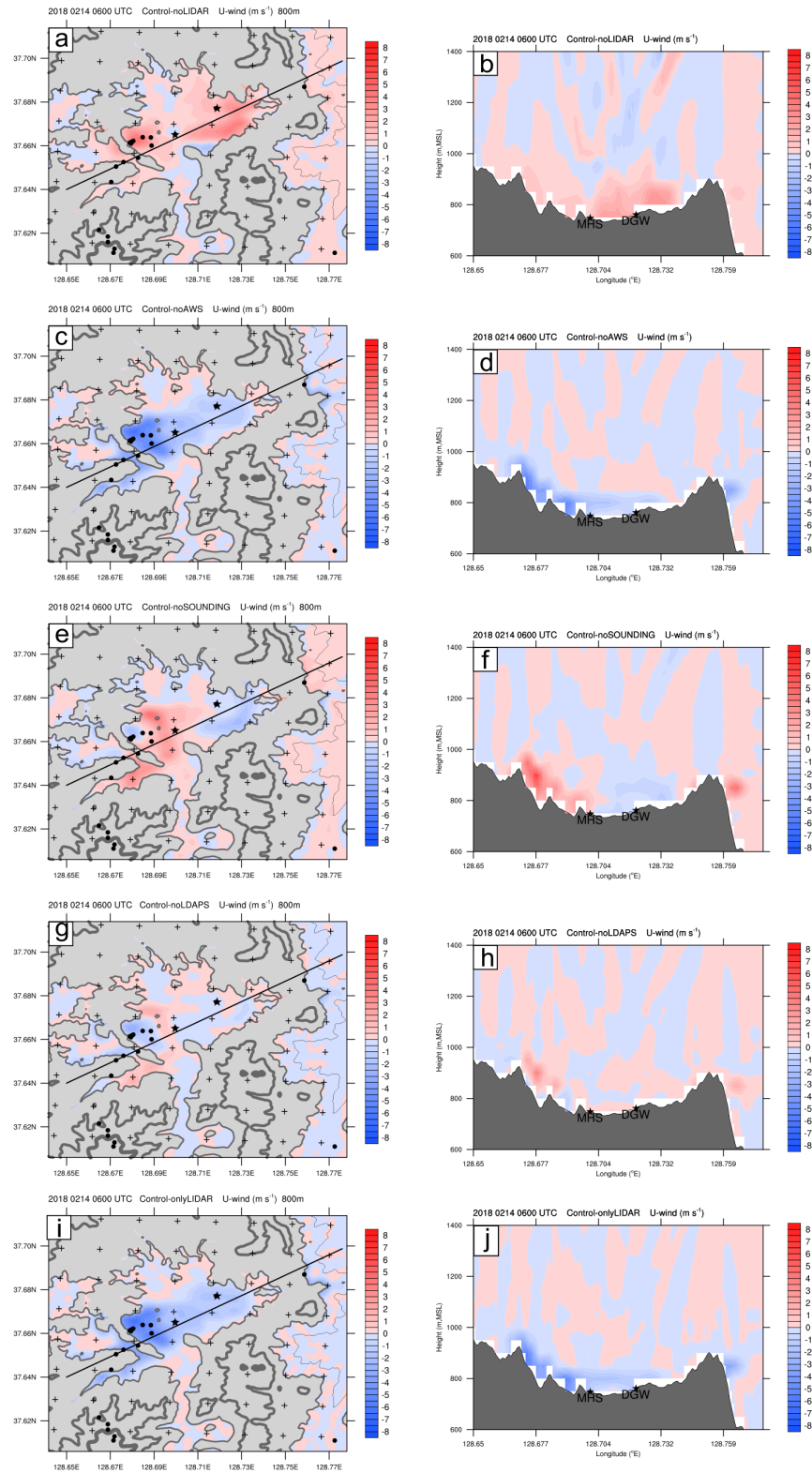
Figure 12. (a) The discrepancies in horizontal u-component winds between the control run and A-1 at 800 m MSL

635

636   at 06:00 UTC on 14 Feb. 2018. (b) The same as (a) but for the vertical section along the black line in (a). (c) and

637   (d) are the same as (a) and (b) but for A-2. (e) and (f) are the same as (a) and (b) but for A-3. (g) and (h) are the

638   same as (a) and (b) but for A-4. (i) and (j) are the same as (a) and (b) but for A-5.

639

640   Averaged discrepancies ~~of~~ in derived 3D winds for each vertical level in entire domain are

641 shown in Fig. 13a. These results summarized a series of sensitivity tests if the WISSDOM

642 synthesis lacks certain data inputs (i.e., A-1~A-~~4~~5 in Experiment A) for derived u-, v- and w-

643 component winds in the test domain. Overall, the maximum absolute value of averaged

644 discrepancies for Experiment A are smaller than approximately 0.5 m s^{-1}, which are the

645 discrepancies of the u-component winds for A-1 and A-2 located at 800 m MSL. Except for these

646 values, the values of the derived u-, v- and w-component winds for A-1~A-2 are approximately

647 smaller than 0.2 m s^{-1} from the surface up to the top in the test domain. Based on the results of

648 A-5, relatively stronger values of derived u-component (exceeded -0.4 m s^{-1} at lower layers) can

649 be obtained from the setting like old version of WISSDOM. The wind speed can be better

650 modulated in modified version of WISSDOM when the Doppler lidar observations were adopted.

651 ~~These results also implied that the ranges of errors are relatively small when we try to evaluate~~

652 ~~the discrepancies between the control run and each independent observation~~.

653   In addition, the discrepancies in derived 3D winds between sounding observations and QVP

654 were also examined along the sounding tracks (Fig. 13b) and above the DGW site (Fig. 13c).

655 Sounding observations played an essential role in the derived winds along its tracks. The

656 maximum discrepancies of u- (v-) component winds are exceeded by approximately -2 (-1) m

657 s^{-1} if the WISSDOM synthesis lacks sounding observations. However, small discrepancies

658 (nearly 0 m s^{-1}) were presented when the sounding (lidar) data were (not) implemented at all

659 levels in A-1. The peaks in the discrepancies manifested the potential impacts from the lidar and

660 AWS. This may be a result of lidar (AWS) having relativity higher data coverage at ~1.4 (0.8)

661 km MSL (cf. Fig. 4). The maximum discrepancies between the derived winds and the QVP winds

662 are approximately -4 and 4 (-1 and 0) m s^{-1} associated with u-, v- (w-) component winds.

663 Generally, the results reveal similar trends in A-1~A-5, which also implies that all the inputs in

664 the WISSDOM synthesis are equally significant against the QVP. ~~–~~In summary, the results of

665 this experiment (cf. Fig. 13) ~~concluded~~ show that the lidar, sounding, and AWS data are more

666 critical inputs in modified WISSDOM., Therefore, iand it will be benefitbeneficials if more

667 various inputs can be included in the synthesis.

668
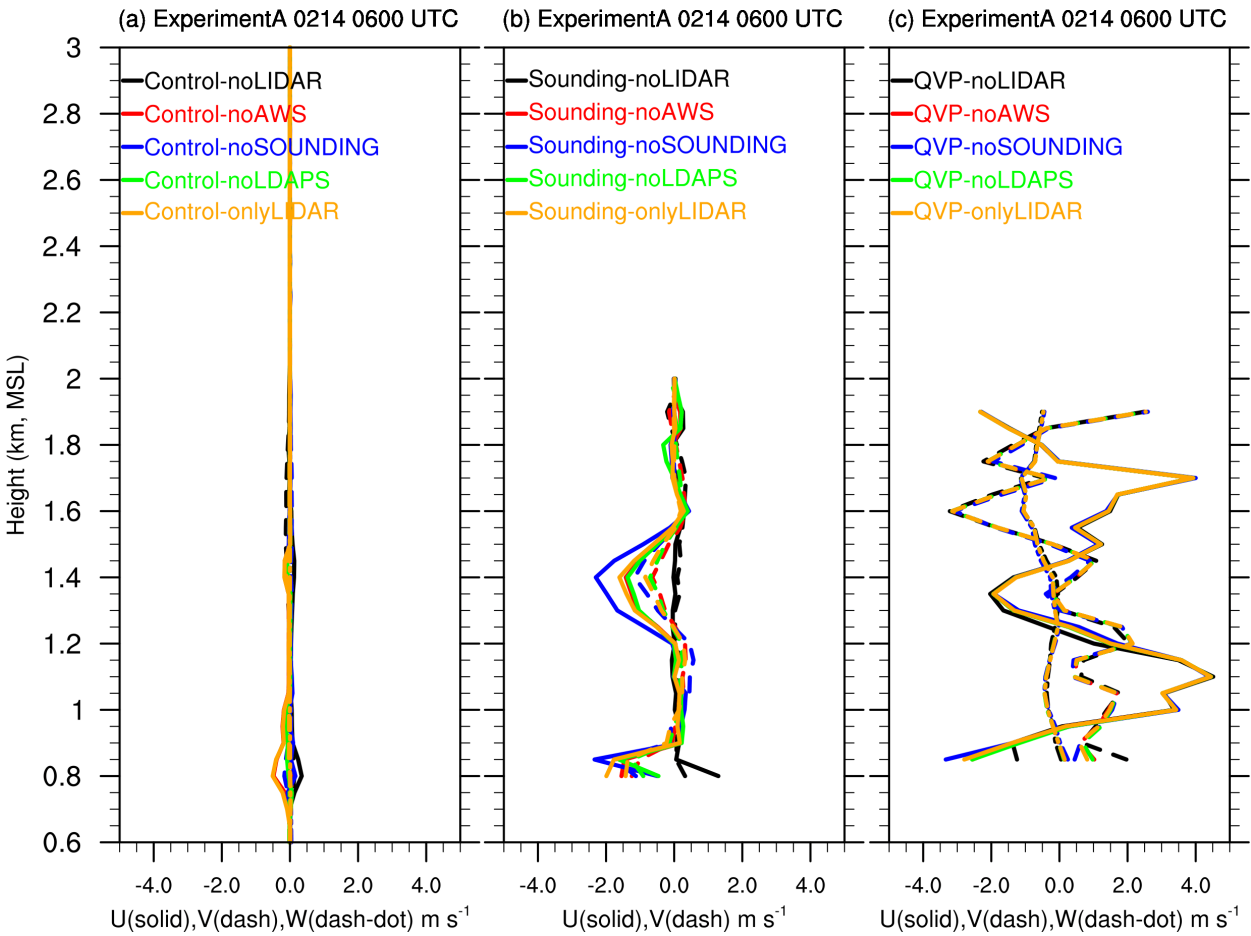
669 Figure 13. (a) Vertical profiles of averaged discrepancies of 3D winds for each design in Experiment A at 06:00
670 UTC on 14 Feb. 2018. The averaged discrepancies of u-, v- and w-component winds were plotted by solid, dash,
671 and dash-dot lines, and the black, red, blue, green and orange lines indicate A-1, A-2, A-3, A-4 and A-5,
672 respectively. (b) The same as (a) but for the discrepancies of sounding observations and u-, and v-component
673 winds. (c) The same as (a) but for the discrepancies of QVP.

674 **5.2 Radius of influence (RI) and vertical extension for the AWS (Experiment B)**

675 Experiment B was performed to check the discrepancies in 3D winds between the control run

676 and the different settings of RI and VE with the AWS observations. Because the average distance

677 is approximately 0.1 to 2 km between each AWS site, tThere were five designs (B-1~B-5) in

678 Experiment B with the ranges of RI (VE) between 0.5 km (50%) and 2 km (90%). Because the

679 average distance between each AWS site is approximate from 0.1 to 2 km and more data can be

680 ~~included in vertically.~~ The details are shown in Table 4. The horizontal u-component winds at

681 800 m MSL and the vertical structure of Experiment B at one time step (06:00 UTC on 14

682 February 2018) are shown in Fig. 14. An unusual circular area with positive discrepancies around

683 the MHS site was depicted in B-1 (Figs, 14a and 14b), which may have been produced by the

684 insufficient RI distance and VE (the circular artefact is removed when increasing VE to

685 90%)~~unusual circle can be vanished when VE becoming 90%)~~. Relatively smaller RI and VE

686 values can only include relatively less wind information if the distances are large between each

687 AWS ~~station~~. Enlarging the RI and VE are required to appropriately include more wind

688 information from the AWS observations. Figs. 14c and 14d show the results of B-2 as VE reached

689 90%. Although the unusual circle vanished, there were discontinuities with negative values near

690 the northern and southern areas of the MHS site and positive areas surrounding the AWS

691 (128.68°E, 37.66°N). The setting of B-3 was similar to that of the control run except that the VE

692 was 50%. The discrepancies were relatively small, albeit dense AWS ~~stations~~ contributed even

693 smaller negative values in the western areas of the MHS sites (Figs. 14g and 14h). Obviously,

694 positive discrepancies appeared near the northern and southern areas of the MHS site in B-4 and

695 B-5 (Figs. 14g-j). The impacts of the AWS with various settings (B-1~B-5) on the discrepancies

696 in u-component winds were both restricted near the surface, even with a larger RI and high VE.

697
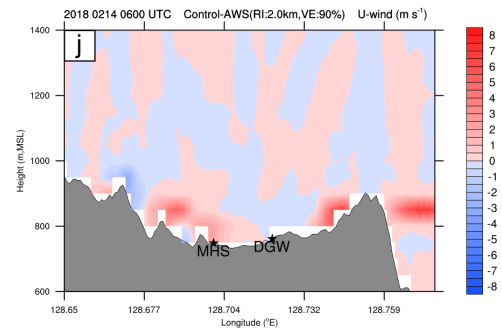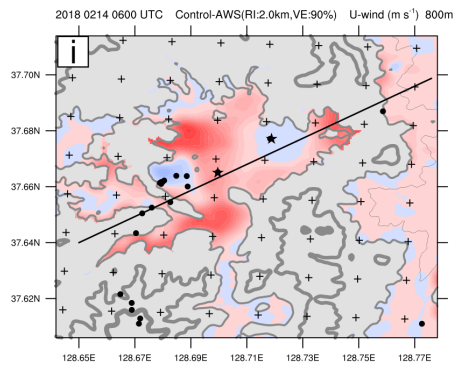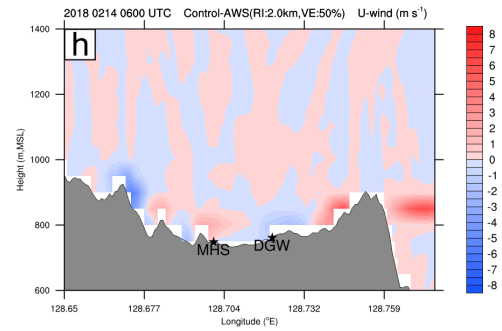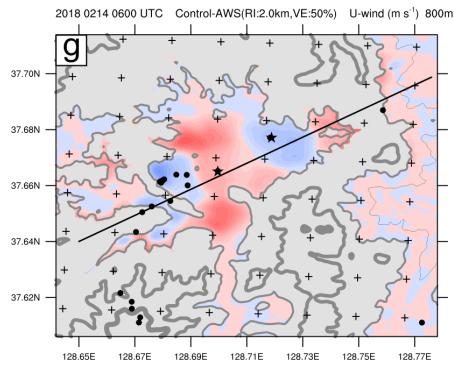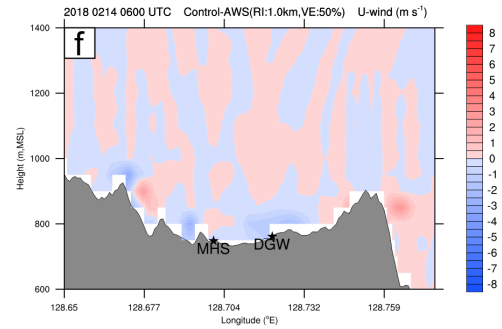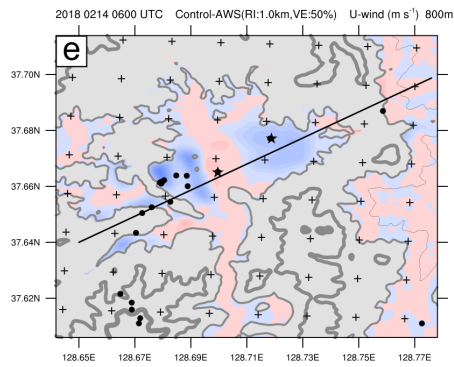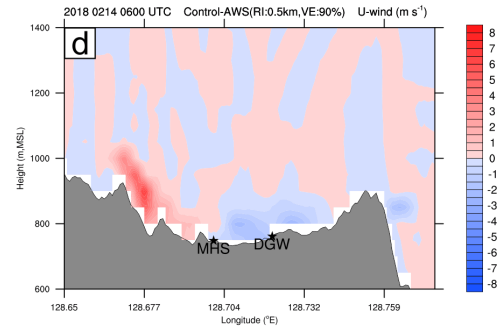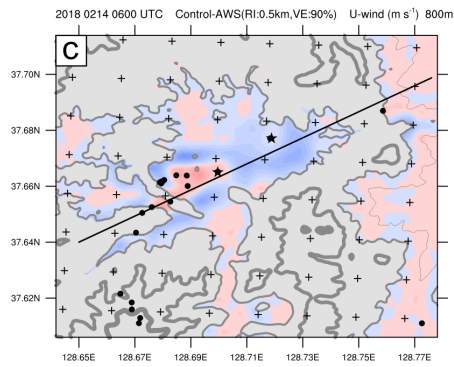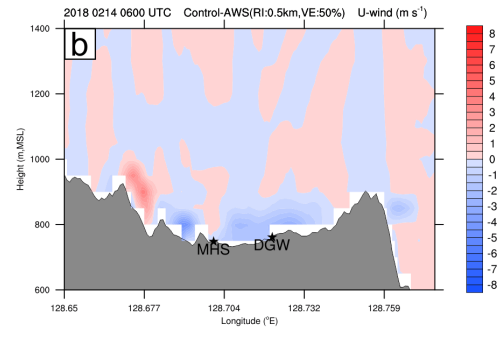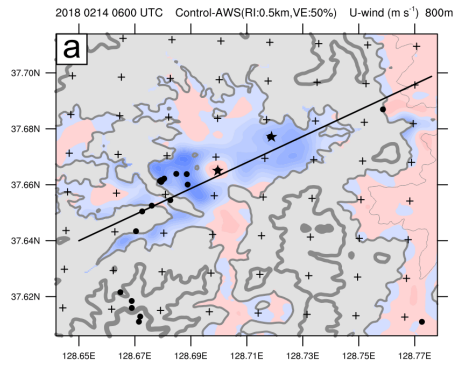
Figure 14. The same as Fig.12, but (a) and (b) for B-1. (c) and (d) are the same as (a) and (b) but for B-2. (e) and (f) are the same as (a) and (b) but for B-3. (g) and (h) are the same as (a) and (b) but for B-4. (i) and (j) are the same as (a) and (b) but for B-5.

Fig. 15a shows the vertical profiles of averaged discrepancies of derived 3D winds in Experiment B. This figure summarizes the results of sensitivity testing with different settings of the RI and VE in WISSDOM (i.e., B-1~B-5 in Experiment B, shown in Table 4) for derived u-, v- and w-component winds in the test domain. The maximum discrepancies of u-component winds in B-1, B-2 and B-3 were quite small at only 0.4, 0.3 and 0.2 m s^{-1}, respectively. Nevertheless, the maximum discrepancies of u-component winds for B-4 and B-5 were larger than 0.6 m s^{-1} and even exceeded ~1 m s^{-1}. Although the discrepancies in the u-component winds in B-1 were small, the discrepancies in the v-component winds in B-1 reveal unusual patterns, with larger positive values at ~1100 m MSL and negative values at ~1800 m MSL (black dashed line in Fig. 15a), the possible reason is the minimizations of cost function are not converged well because relatively few and weak v-component winds were included in B-1. Except for this value, the maximum discrepancies of v-component winds were small for B-2~B-5, and the maximum discrepancies of w-component winds were also small for all of Experiment B. Note that B-3 always has the smallest discrepancies with the derived 3D winds because the setting is quite similar to the control run. Figs. 15b and 15c show the discrepancies of derived 3D winds between the sounding observations and QVP. Their patterns are similar to A-1~A5 (cf. Figs. 13b and 13c), except there were relatively larger values of u- (v-) component winds at lower layers (approximately −3 and 1 m s^{-1}) in B-1 (Fig. 15b). The v-component winds also presented larger values (exceeded ~3 m s^{-1}) below ~1.2 km MSL compared with the QVP (Fig. 15c). The conclusions indicated that the moderate setting (i.e., RI is 1 km) ~~will~~ would be helpful to ~~get~~ ~~the~~obtain ~~smallest~~ minor differences with the control run, sounding observations and the QVP. On the other hand, the limited setting in experiment B (i.e., B-1) was helpless. In addition, the wind directions and speed should be ~~more~~ dominated by terrain~~s at lower layers~~, and the

724 ~~implement~~implementations of AWS data ~~are~~ is ~~very important~~crucial for the modified

725 WISSDOM synthesis, especially ~~at~~ in the lower layers~~the height below 900 m MSL~~.

726
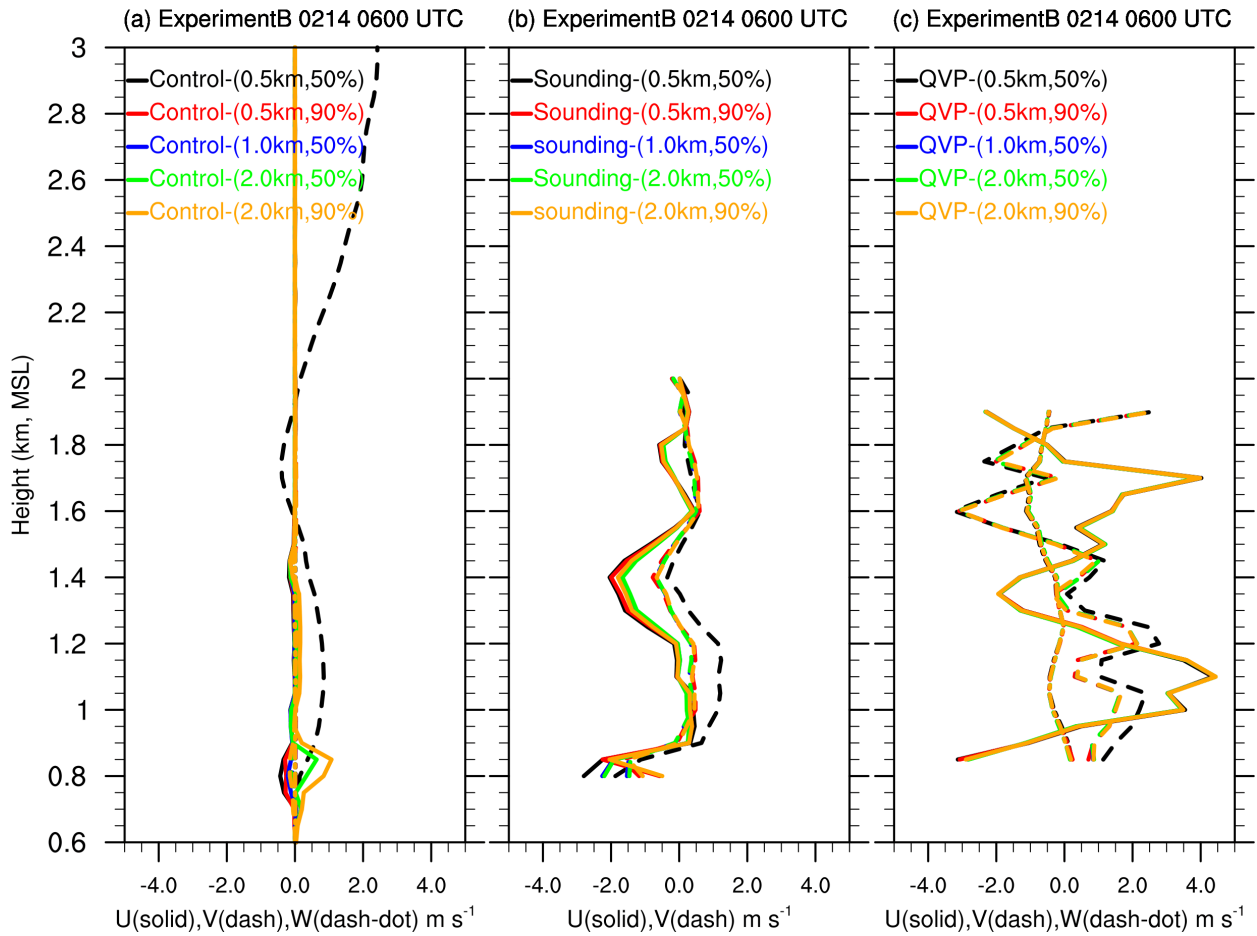
727 Figure 15. The same as Fig. 13. but for B-1~B-5.

5.3 Different weighting coefficients for the constraints (Experiment C)

729   Experiment C was designed to check the discrepancies in the derived u-component winds

730 between the control run and experimental runs with different weighting coefficients for each

731 constraint related to the AWS, lidar and LDAPS (corresponding to C-1, C-2 and C-3 in Table 4).

732 Originally, the weighting coefficients for the AWS and lidar observations were set to 10^6, and the

733 value was 10^3 for the LDAPS dataset (i.e., control run, Table 1). The results of Experiment C

734 show significant negative discrepancies in u-component winds near the surface in C-1, especially

735 in the areas next to the AWS (128.68°E, 37.66°N). The discrepancies for C-1 (Figs. 16a and 16b)

736 and C-2 (Figs. 16c and 16d) are similar to those for A-2 (Figs. 12c and 12d) and A-1 (Figs. 12a

737 and 12b), respectively. The inputs of AWS and lidar both contributed relatively weak impacts to

738 the WISSDOM synthesis when the weighting coefficient was set to 10^3. Irrational patterns were

739 depicted when the weighting coefficient of LDAPS inputs increased to 10^6, and larger and

740 positive discrepancies were crowded into most areas in the valley (i.e., C-3, Figs. 16e). Larger

741 and positive discrepancies existed only near the surface, and there were negative discrepancies

742 between approximately 1000 m and 1400 m (Fig. 16f). Notably, significant variances usually

743 existed between the observations and reanalysis datasets due to various spatiotemporal

744 resolutions. The results of scenario C-3 do not converge well because there was a relatively more

745 significant gradient between each input as their weighting coefficients were set to be the same

746 (i.e., 10^6). In this way, the effects of poor convergences might be amplified and superposed with

747 the AWS and lidar observations along the sounding tracks. ~~Note that~~ This may be a possible

748 reason that artificial signals existed ~~the influences of sounding observations also existed above~~

749 over the DGW site in scenario C-3.~~.~~ ~~————~~

750 The vertical profiles of averaged discrepancies of derived 3D winds in Experiment C are

751 shown in Fig. 17a. Absolute values of the discrepancies in the u-, v- and w-component winds are

752 smaller than 1 m s^{-1}, except for the discrepancies in the v-component winds with low weighting

753 of the AWS observations (i.e., C-1) and the discrepancies in the u- and v-component winds with

754 the high weighted LDAPS (i.e., C-3). The discrepancies in the v-component winds in C-1

755 exceeded -5 m s^{-1} at ~1100 m MSL and were larger than -15 m s^{-1} above 2600 m MSL. These

756 unreasonable characteristics are also shown as the discrepancies in the v-component winds in B-

757 1 (cf. Fig. 15a). The discrepancies in the u- and v-component winds in C-3 are 15 m s^{-1} and 4 m

758 s^{-1}, respectively, in the layers between 700 and 900 m MSL. Alternative positive and negative

759 discrepancies in the range of $-$3 to 3 m s^{-1} for the u-component winds in C-3 were found above

760 1000 m MSL.

761 The discrepancies in derived 3D winds between sounding observations and QVP in

762 Experiment C were also examined. Compared to the sounding observations, more significant

763 discrepancies in the u- and v-component winds (exceeded ~20 m s^{-1}) can be obtained when

764 reducing (increasing) the weighting coefficients of the AWS (LDAPS) data (Fig. 17b). However,

765 the impacts of lidar against the QVP are shown; their discrepancies are in the range of −1 to 2 m

766 s^{-1} for the u-component winds in C-2 (Fig. 17c). The conclusions reveal that the weighting

767 coefficients of the AWS and LDAPS (lidar) are (moderately) significantly sensitive to the derived

768 winds. Therefore, the weighting coefficients of LDAPS and AWS are not necessarily changed

769 much~~The conclusions reveals that the weights of the AWS and LDAPS (lidar) are (not) too~~

770 ~~sensitive to the derived winds. Therefore, the weights of LDAPS and AWS are not necessary~~

771 ~~changed too much~~.

772
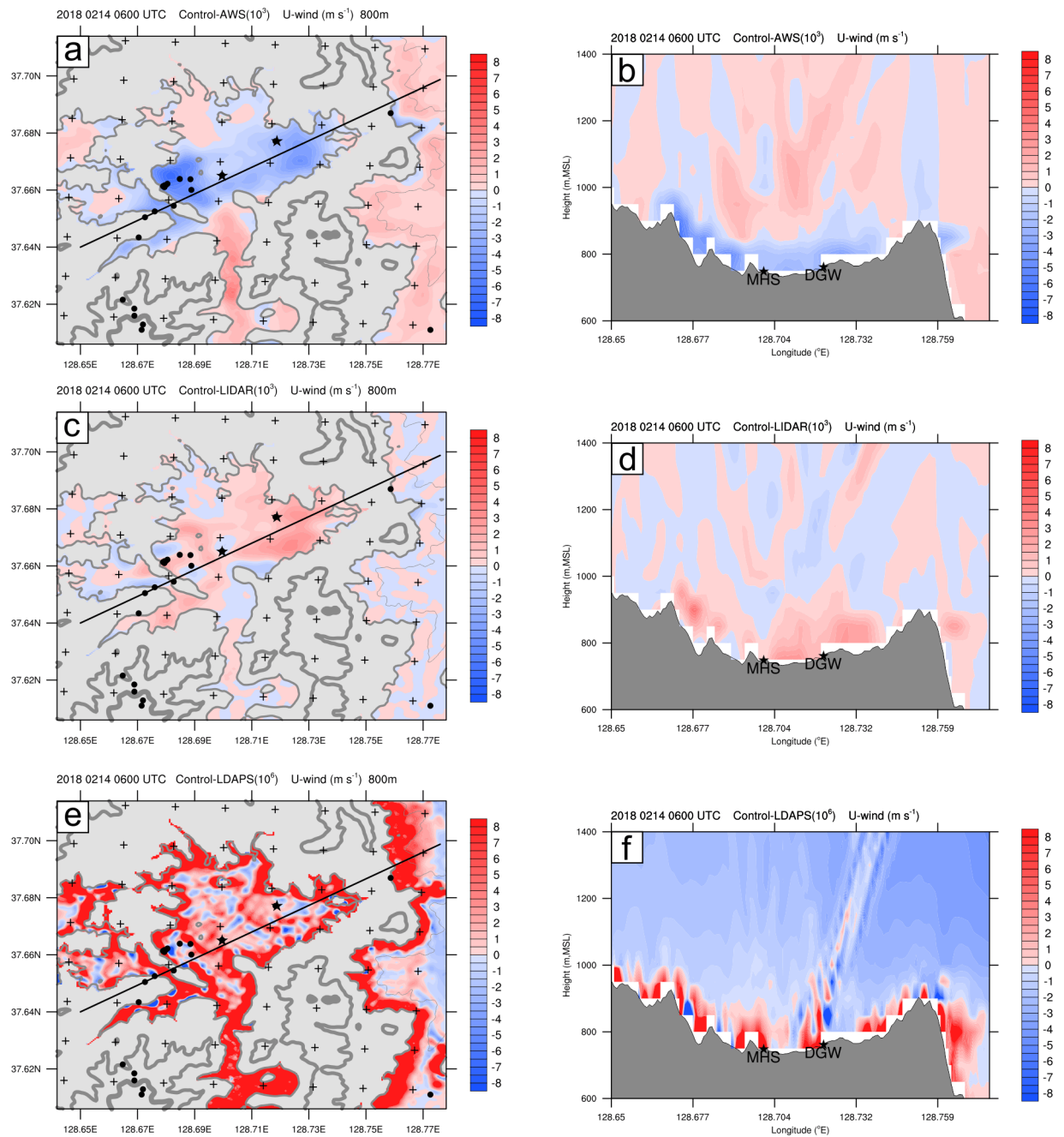
773 Figure 16. The same as Fig.12, but (a) and (b) for C-1. (c) and (d) are the same as (a) and (b) but for C-2. (e) and (f)

774   are the same as (a) and (b) but for C-3.
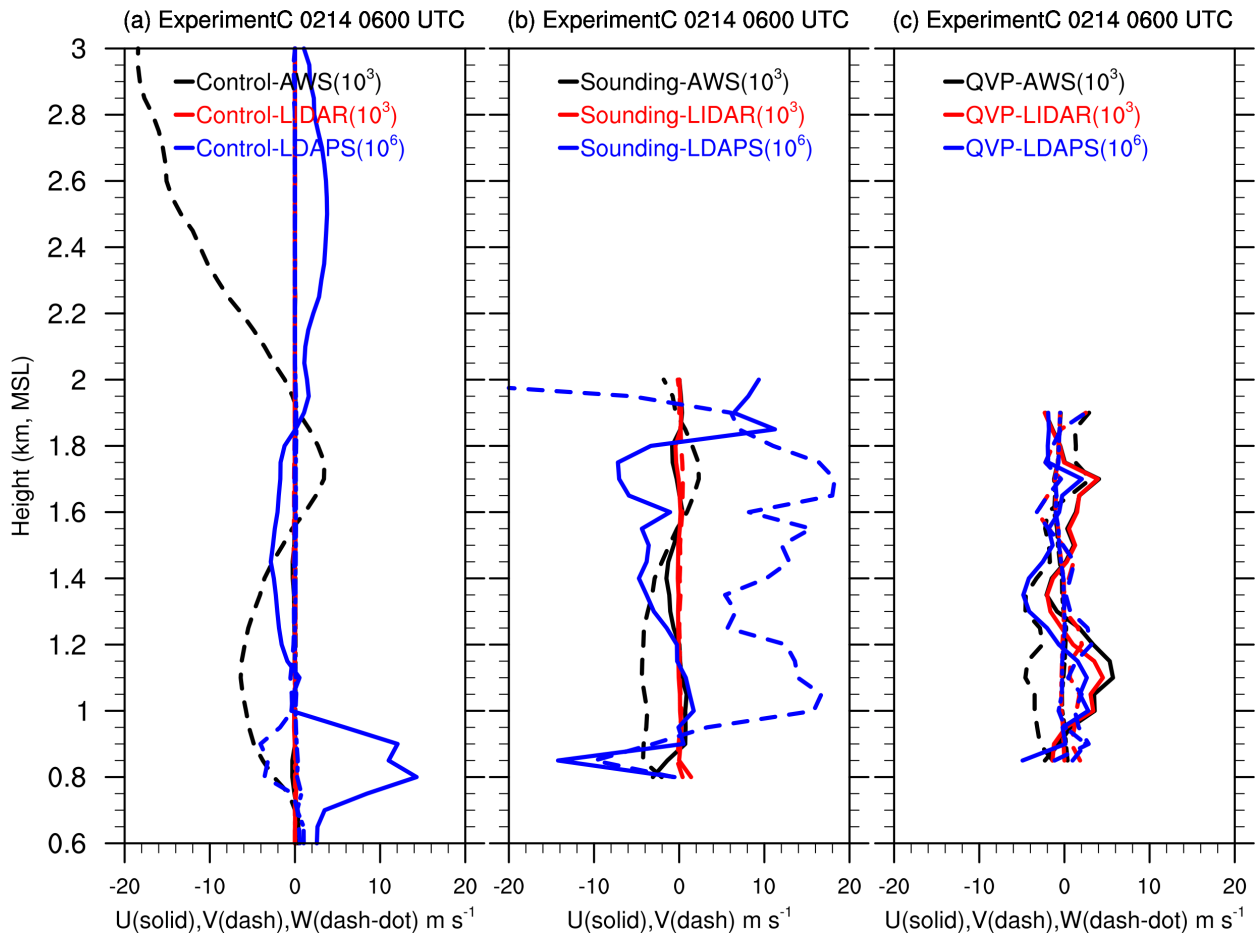
Figure 17. The same as Fig. 13 but for C-1~C-3.

6. Conclusion

A modified WISSDOM synthesis scheme was developed to derive high-quality 3D winds under clear-air conditions. The main difference from the original version is that multiple lidar observations were used, and high-resolution 3D winds (50 m horizontally and vertically) were first derived in the modified WISSDOM scheme. In addition, all available datasets were included as one of the constraints in the cost function in this study. The data implementation and the detailed principles of the modified WISSDOM were also elaborated. This modified WISSDOM scheme was performed over the TMR to retrieve 3D winds during a strong wind event during ICE-POP 2018. The performance was evaluated via a series of sensitivity tests and compared with conventional observations.

787   The intercomparisons of horizontal winds during the entire research period reveal a relatively

788   high correlation coefficient between the optimal results of WISSDOM synthesis and sounding's

789   u- (v-) component winds exceeding 0.97 (0.87) at the DGW site. Furthermore, the average bias

790   is -0.78 m s^{-1} (0.09 m s^{-1}), and the RMSD is 1.77 m s^{-1} (1.65 m s^{-1}) for the u- (v-) component

791   winds. The intercomparisons of 3D winds between the WISSDOM synthesis and lidar QVP also

792   showed a higher correlation coefficient (0.84) for u-component winds, but a relatively smaller

793   correlation coefficient remained at 0.35 for v-component winds in this strong wind event. The

794   average bias (RMSD) of u-component winds is 2.83 m s^{-1} (3.69 m s^{-1}), and the average bias and

795   RMSD of v-component winds are 2.26 m s^{-1} and 2.92 m s^{-1}, respectively (cf. Table 2). Chen

796   (2019) analyzed the correlations between 3D winds derived from radar and observations in

797   several typhoon cases; the mean correlation coefficient ranged from 0.56 to 0.86, and the RMSD

798   was between 1.13 and 1.74 m s^{-1}. Compared to their results, only u-component winds have

799   relatively higher correlation coefficients, but the RMSD values are slightly higher in this study,

800   which may have been caused by the high variability in westerly winds associated with the moving

801   LPS. The statistical error results of the winds between the optimal results of WISSDOM synthesis

802   and observations show a good performance of the retrieved 3D winds in this strong wind event

803   (Table 3). Generally, the median values of wind directions are within ~10 degrees. Compared

804   with lidar QVP (sounding observations) the median values of the wind speed are approximately

805   -1~3 m s^{-1} (-1~0.5 m s^{-1}) and the vertical velocity is within -0.2~0.6 m s^{-1}. Compared with

806   lidar QVP (sounding observations) above the DGW site, the interquartile range of wind directions

807   is -10~5 (0-2.5) degrees, the wind speed is approximately -4~4 m s^{-1} (-1~3 m s^{-1}) and the

808   vertical velocity is -0.8~0.8 m s^{-1}. The summaries of the correlation coefficients, average bias,

809   the RMSD, and range of statistical errors are shown in the schematic diagrams as Figs. 18a

810   and 18b.
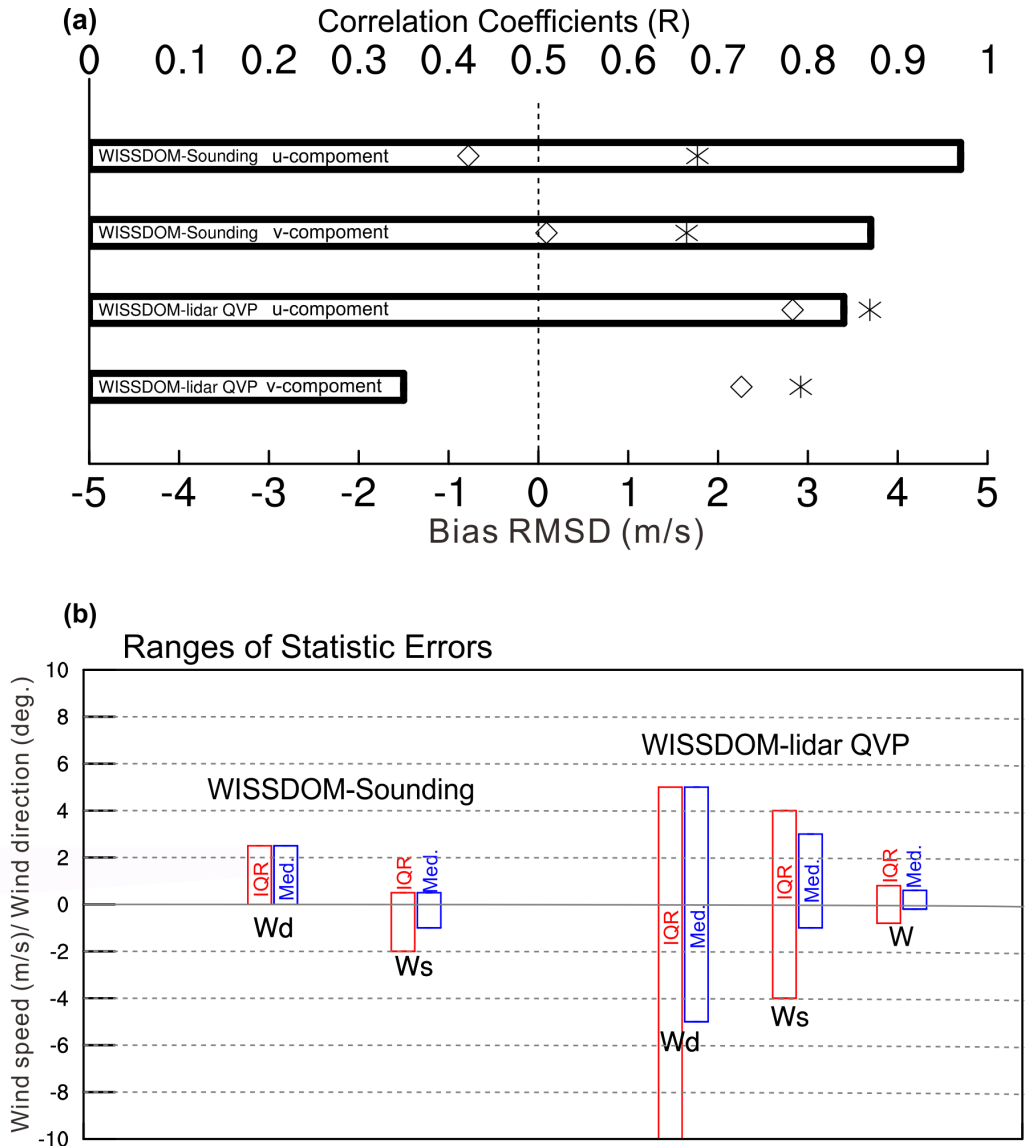
812 Figure 18. Schematic diagrams for the results of intercomparisons on (a) the correlation coefficients (R, histograms),

813 the average bias (marked as diamonds), and the RMSD (marked as asterisks). (b) The ranges of statistic error for

814 the IQR (red boxes) and median values (blue boxes). The wind directions, and wind speed and w-component

815 winds are denoted as Wd, and Ws, and W respectively.

816   A control run (see the basic setting in Table 1) was set to explore the importance of acquired

817 observation datasets, various distances of RI, VE from the AWS observations, and the weighting

818 coefficient for each constraint (i.e., Experiments A-C, Table 4). The results of Experiment A

819 show that the lidar and AWS play critical roles in the derived horizontal winds, and the lidars

820 (AWS) provided positive (negative) contributions in stronger (weaker) wind speeds near the

821 surface. The sounding and the LDAPS provided relatively smaller impacts on the derived

822 horizontal winds from the WISSDOM synthesis. In Experiment B, the smallest minor

823   discrepancies in 3D winds were depicted when the RI (VE) was set to 1 km (50%)~~,;~~ which~~it~~

824   indicated that the optimal setting of the RI is 1 km. However, there were larger discrepancies in

825   3D winds (from −0.4 m s^{-1} to ~1 m s^{-1}) when the RI was set at 0.5 km and 2 km, and the VE was

826   set between 50% and 90% (cf. Fig. 15). In Experiment C, significant discrepancies in 3D winds

827   appeared by decreasing (raising) the weighting coefficient from the AWS observations (LDPAS

828   datasets). ~~In addition to the~~Relatively reasonable winds can be derived ~~by applying the~~

829   ~~optimal~~with optimal setting~~s~~ in modified WISSDOM, and the setting of 90% (50%) ~~of~~in VE ~~are~~

830   is also recommended over complex terrain (flat surface). ~~The results of T~~these sensitivity test~~s~~

831   ~~ing~~will ~~be~~ help~~ful to verify~~ verify the impacts ~~from~~ against various scenarios and observational

832   references in this area. The conclusions can also be a good ~~refence~~reference ~~to decide~~for deciding

833   ~~where~~ the best locations to ~~for~~deploy the instruments ~~employed~~.

834   This study demonstrated that reasonable patterns of 3D winds were derived by the modified

835   WISSDOM synthesis scheme in a strong wind event. Reasonable winds can be retrieved from

836   modified WISSDOM with sufficient coverage from the data, a moderate weighting function, and

837   appropriate ~~implement~~implementation~~s~~ from different datasets. In the future, many cases are

838   required to check the performance of this modified WISSDOM scheme with different synoptic

839   weather systems under clear-air conditions in different seasons. In addition, knowing the detailed

840   kinematic fields will help us to identify where the flow accelerates/decelerates over complex

841   terrain. Thus, the possible mechanisms of extremely strong winds in South Korea will be well

842   documented through combinations with derived dynamic fields (Tsai et al., 2018, 2022),

843   thermodynamic fields (Liou et al., 2019), observations and simulations. ~~Except for t~~The detailed

844   wind structures can be well documented ~~in~~ for any meteorological phenomena ~~under~~ in clear-air

845   conditions (e~~.g~~g., land~~–~~-sea breeze~~s~~, micro~~-~~downburst~~s~~, ~~and~~ non~~-~~precipitation low-pressure

846   systems, etc.) via a modified~~. Furthermore, the new~~ version of WISSDOM. It also has broad

847   applications in site surveys of wind turbines, wind energy, monitoring wildfires, outdoor sports

848   in mountain ranges, and aviation security.

849   *Code and data availability.* The scanning Doppler lidars, AWS, and sounding data used in this
850   study are available through zenodo: https://doi.org/10.5281/zenodo.6537507. The LDAPS
851   dataset is freely available from the KMA website (https://data.kma.go.kr).
852
853   *Acknowledgments*. This work was supported by the National Research Foundation of Korea (NRF)
854   grant funded by the Korea government (MSIT) (No. 2021R1A4A1032646) and by the Korea
855   Meteorological Administration Research and Development Program under Grant KMI2022-
856   00310.
857
858   *Author contributions.* This work was made possible by contribution from all authors.
859   Conceptualization, CLT, GWL; methodology, CLT, YCL, and KK; software, CLT, YCL, and
860   KK; validation, KK, YCL, and GWL; formal analysis, CLT, and KK; investigation, CLT, and
861   GWL; writing—original draft preparation, CLT; writing—review and editing, GWL, YCL and
862   KK; visualization, CLT; supervision, GWL; funding acquisition, GWL. All authors have read
863   and agreed to the published version of the manuscript.
864
865   *Competing interests.* The authors declare that they have no conflict of interest.
866
867   *Special issue statement.* This article is part of the special issue "Winter weather research in
868   complex terrain during ICE-POP 2018 (International Collaborative Experiments for
869   Pyeongchang 2018 Olympic and Paralympic winter games) (ACP/AMT/GMD inter-journal SI)".
870   It is not associated with a conference.
871
872

References

Armijo, L.: A theory for the determination of wind and precipitation velocities with Doppler radars. J. Atmos. Sci., 26, 570–573. 1969.

Bell, M. M., Montgomery, M. T., and Emanuel, K. A.: Air–sea enthalpy and momentum exchange at major hurricane wind speeds observed during CBLAST, *J. Atmos. Sci.*, **69**, 3197–3222, https://doi.org/10.1175/JAS-D-11-0276.1, 2012.

Bell, T. M., Klein, P., Wildmann, N., and Menke, R.: Analysis of flow in complex terrain using multi-Doppler lidar retrievals, *Atmos. Meas. Tech.*, **13**, 1357–1371, https://doi.org/10.5194/amt-13-1357-2020, 2020.

Browning, K. A., and Wexler, R..: The Determination of Kinematic Properties of a Wind Field Using Doppler Radar, *J. Appl. Meteorol.*, **7**, 105–113, https://doi.org/10.1175/1520-0450(1968)007<0105:TDOKPO>2.0.CO;2, 1968.

Chen, Y.-A.: Verification of multiple-Doppler-radar derived vertical velocity using profiler data and high resolution examination over complex terrain, M.S. thesis, National Central University, 91 pp., 2019.

Choi, D., Hwang, Y., Lee, YH.: Observing Sensitivity Experiment Based on Convective Scale Model for Upper-air Observation Data on GISANG 1 (KMA Research Vessel) in Summer 2018. *Atmosphere*, **30**, 17–30, 2020 (Korean with English abstract).

Cha, T.-Y. and Bell, M. M.: Comparison of single-Doppler and multiple-Doppler wind retrievals in Hurricane Matthew (2016), *Atmos. Meas. Tech.*, **14**, 3523–3539, https://doi.org/10.5194/amt-14-3523-2021, 2021.

Choukulkar, A., Brewer, W. A., Sandberg, S. P., Weickmann, A., Bonin, T. A., Hardesty, R. M., Lundquist, J. K., Delgado, R., Iungo, G. V., Ashton, R., Debnath, M., Bianco, L., Wilczak, J. M., Oncley, S., and Wolfe, D.: Evaluation of single and multiple Doppler lidar techniques to measure complex flow during the XPIA field campaign, *Atmos. Meas. Tech.*, **10**, 247–264, https://doi.org/10.5194/amt-10-247-2017, 2017.

899   Colle, B. A., and Mass, C. F.: High-Resolution Observations and Numerical Simulations of

900   Easterly Gap Flow through the Strait of Juan de Fuca on 9–10 December 1995. *Mon. Wea.*

901   *Rev.*, **128**, 2398–2422,

902   Cressman, G. P.: An operational objective analysis system. *Mon. Wea. Rev.*, **87**, 367–374, 1959.

903   Gao, J., Droegemeier, K. K., Gong, J., and Xu, Q.: A method for retrieving mean horizontal wind

904   profiles from single-Doppler radar observations contaminated by aliasing, *Mon. Wea.*

905   *Rev.*, **132**, 1399–1409, https://doi.org/10.1175/1520-

906   0493(2004)132<1399:AMFRMH>2.0.CO;2, 2004.

907   Hill, M., R. Calhoun, H. J. S. F., Wieser, A., Dornbrack, A., Weissmann, M., Mayr, G., and

908   Newsom, R.: Coplanar Doppler lidar retrieval of rotors from T-REX, *J. Atmos. Sci.*, **67**,

909   713–729, 2010.

910   Jou, B. J.-D., Lee, W.-C., Liu, S.-P., and Kao, Y.-C.: Generalized VTD retrieval of atmospheric

911   vortex kinematic structure. Part I: Formulation and error analysis, *Mon. Weather Rev.*,

912   **136**, 995–1012, https://doi.org/10.1175/2007MWR2116.1, 2008.

913   Kim D.-J., Kang G., Kim D.-Y., Kim J.-J.: Characteristics of LDAPS-Predicted Surface Wind

914   Speed and Temperature at Automated Weather Stations with Different Surrounding Land

915   Cover and Topography in Korea. *Atmosphere*, **11**, 1224.

916   https://doi.org/10.3390/atmos11111224, 2020.

917   Kim, J.-H., R. D. Sharman, R. D., Benjamin, S., Brown, J., Park, S.-H. and Klemp, J.:

918   Improvement of Mountain Wave Turbulence Forecast in the NOAA's Rapid Refresh

919   (RAP) Model with Hybrid Vertical Coordinate System, *Weather Forecast*, **34(6)**, 773-

920   780, https://doi.org/10.1175/WAF-D-18-0187.1, 2019.

921   Kim, K., Lyu, G., Baek, S., Shin, K., and Lee, G.: Retrieval and Accuracy Evaluation of

922   Horizontal Winds from Doppler Lidars during ICE-POP 2018, *Atmos.*, **32**, 163–178,

923   https://doi.org/10.14191/Atmos.2022.32.2.161, 2022.

924   Lee, J., Seo, J., Baik, J., Park, S., and Han, B.: A Numerical Study of Windstorms in the Lee of

the Taebaek Mountains, South Korea: Characteristics and Generation Mechanisms. *Atmosphere*, **11**, 431. https://doi.org/10.3390/atmos11040431, 2020.

Lee, J.- T., Ko, K.- Y., Lee, D.- I., You, C.- H., and Liou, Y.- C.: Enhancement of orographic precipitation in Jeju Island during the passage of Typhoon Khanun (2012), *Atmos. Res.*, **201**, 1245–1254. https://doi.org/10.1016/j.atmosres.2017.10.013, 2017.

Lee, W.-C., Marks, F. D., and Carbone, R. E.: Velocity track display – A technique to extract real-time tropical cyclone circulations using a single airborne Doppler radar, *J. Atmos. Ocean. Tech.*, **11**, 337–356, https://doi.org/10.1175/1520-0426(1994)011<0337:VTDTTE>2.0.CO;2, 1994

Lee, W.-C., Jou, B. J.-D., Chang, P.-L., and Deng, S.- M.: Tropical cyclone kinematic structure derived from single-Doppler radar observations. Part I: Interpretation of Doppler velocity patterns and the GBVTD technique, *Mon. Weather Rev.*, **127**, 2419–2439, https://doi.org/10.1175/1520-0493(1999)127<2419:TCKSRF>2.0.CO;2, 1999.

Liou, Y.-C., Wang, T.-C. C., Lee, W.-C., and Chang, Y.-J.: The retrieval of asymmetric tropical cyclone structures using Doppler radar simulations and observations with the extended GBVTD technique, *Mon. Weather Rev.*, **134**, 1140–1160, https://doi.org/10.1175/MWR3107.1, 2006.

Liou, Y., and Chang, Y.: A Variational Multiple–Doppler Radar Three-Dimensional Wind Synthesis Method and Its Impacts on Thermodynamic Retrieval. *Mon. Wea. Rev.*, **137**, 3992–4010, https://doi.org/10.1175/2009MWR2980.1, 2009.

Liou, Y., Chang, S., and Sun, J.: An Application of the Immersed Boundary Method for Recovering the Three-Dimensional Wind Fields over Complex Terrain Using Multiple-Doppler Radar Data. *Mon. Wea. Rev.*, **140**, 1603–1619, https://doi.org/10.1175/MWR-D-11-00151.1, 2012.

Liou, Y., Chen Wang, T., Tsai, Y., Tang, Y., Lin, P., and Lee, Y.: Structure of precipitating systems over Taiwan's complex terrain during Typhoon Morakot (2009) as revealed by weather

951   radar and rain gauge observations, *J. Hydrology*, **506**, 14-25.

952   https://doi.org/10.1016/j.jhydrol.2012.09.004, 2013.

953 Liou, Y., Chiou, J., Chen, W., and Yu, H.: Improving the Model Convective Storm Quantitative

954   Precipitation Nowcasting by Assimilating State Variables Retrieved from Multiple-

955   Doppler Radar Observations. *Mon. Wea. Rev.*, **142**, 4017–4035,

956   https://doi.org/10.1175/MWR-D-13-00315.1, 2014.

957 Liou, Y., Chen Wang, T., and Huang, P.: The Inland Eyewall Reintensification of Typhoon

958   Fanapi (2010) Documented from an Observational Perspective Using Multiple-Doppler

959   Radar and Surface Measurements. *Mon. Wea. Rev.*, **144**, 241–261,

960   https://doi.org/10.1175/MWR-D-15-0136.1, 2016.

961 Liou, Y. C., Yang, P. C., and Wang, W. Y.: Thermodynamic recovery of the pressure and

962   temperature fields over complex terrain using wind fields derived by multiple-Doppler

963   radar synthesis. Mon. Wea. Rev., **147(10)**, 3843-3857, https://doi.org/10.1175/MWR-D-

964   19-0059.1, 2019.

965 Mass, C. F., and Ovens, D.: The Northern California Wildfires of 8–9 October 2017: The Role

966   of a Major Downslope Wind Event. *Bull. Amer. Meteor. Soc.*, **100**, 235–256,

967   https://doi.org/10.1175/BAMS-D-18-0037.1, 2019.

968 Mohr, C. G., and Miller, L. J. : CEDRIC—A software package for Cartesian Space Editing,

969   Synthesis, and Display of Radar Fields under Interactive Control. Preprints, *21st Conf. on*

970   *Radar Meteorology,* Edmonton, AB, Canada, Amer. Meteor. Soc., 569–574, 1983.

971 Oue, M., Kollias, P., Shapiro, A., Tatarevic, A., and Matsui, T.: Investigation of observational

972   error sources in multi-Doppler-radar three-dimensional variational vertical air motion

973   retrievals, *Atmos. Meas. Tech.*, **12**, 1999–2018, https://doi.org/10.5194/amt-12-1999-

974   2019, 2019.

975 Park, J.-R., Kim, J.-H., Shin, Y., Kim, S.-H., Chun, H.-Y., Jang, W., Tsai, C.-L. and Lee, G.: A

976   numerical simulation of a strong windstorm event in the Taebaek Mountain Region in

Korea during the ICE-POP 2018, *Atmos. Res.*, **272**, 106158, https://doi.org/10.1016/j.atmosres.2022.106158.

Päschke, E., Leinweber, R., and Lehmann, V.: An assessment of the performance of a 1.5 μm Doppler lidar for operational vertical wind profiling based on a 1-year trial, *Atmos. Meas. Tech.*, **8**, 2251–2266, https://doi.org/10.5194/amt-8-2251-2015, 2015.

Reed, T. R.: GAP WINDS OF THE STRAIT OF JUAN DE FUCA. *Mon. Wea. Rev.*, **59**, 373–376, https://doi.org/10.1175/15200493(1931)59<373:GWOTSO>2.0.CO;2, 1931.

Ryzhkov, A., Zhang, P., Reeves, H., Kumjian, M., Tschallener, T., Trömel, S., and Simmer, C.: Quasi-Vertical Profiles—A New Way to Look at Polarimetric Radar Data. *J. Atmos. Oceanic Technol.*, **33**, 551–562, https://doi.org/10.1175/JTECH-D-15-0020.1, 2016.

Tsai, C., Kim, K., Liou, Y., Lee, G., and Yu, C.: Impacts of Topography on Airflow and Precipitation in the Pyeongchang Area Seen from Multiple-Doppler Radar Observations. *Mon. Wea. Rev.*, **146**, 3401–3424, https://doi.org/10.1175/MWR-D-17-0394.1, 2018.

Tsai, C.-L., Kim, K., Liou, Y.-C., Kim, J.-H., Lee, Y., and Lee, G.: Orographic-induced strong wind associated with a low-pressure system under clear-air condition during ICE-POP 2018, *J. Geophys. Res. Atmos.*, **127**, e2021JD036418. https://doi.org/10.1029/2021JD036418, 2022.

Tseng, Y., and Ferziger, J.: A ghost-cell immersed boundary method for flow in complex geometry. *J. Comput. Phys.*, **192**, 593–623, https://doi.org/10.1016/j.jcp.2003.07.024. 2003.

Yu, C.- K., and Bond, N. A.: Airborne Doppler observations of a cold front in the vicinity of Vancouver Island. Mon. Wea. Rev., 130, 2692-2708, https://doi.org/10.1175/1520-0493(2000)128<1577:ADOOAL>2.0.CO;2, 2002.

Yu, C., and Tsai, C.-L.: Surface Pressure Features of Landfalling Typhoon Rainbands and Their Possible Causes. *J. Atmos. Sci.*, **67**, 2893–2911,_-

1003   ——— https://doi.org/10.1175/2010JAS3312.1, 2010.

1004   Yu, C.-K., & and Tsai, C.-L. : Structural and surface features of arc-shaped radar echoes along

1005   an   outer   tropical   cyclone   rainband. *J.*   *Atmos.*

1006   *Sci.*, **70**, 56– 72. https://doi.org/10.1175/JAS-D-12-090.1, 2013.

1007   Yu, C.-K., and Tsai, C.-L.: Structural changes of an outer tropical cyclone rain band encountering

1008   the topography of northern Taiwan. *Q. J. R. Meteorol. Soc*, **143**, 1107–1122.

1009   https://doi.org/10.1002/qj.2994, 2017.

1010   Yu, C.- K., and Jou, B. J.-D.: Radar observations of diurnally forced, offshore convective lines

1011   along   the   southeastern   coast   of   Taiwan. Mon.   Wea.   Rev., 133,   1613-1636,

1012   https://doi.org/10.1175/MWR2937.1, 2005.–

1013

1014   Yu, C.-K., Cheng, L.-W., Wu, C.-C., and Tsai, C.-L.: Outer Tropical Cyclone Rainbands

1015   Associated with Typhoon Matmo (2014). *Mon. Wea. Rev.*, **148**, 2935–2952,

1016   https://doi.org/10.1175/MWR-D-20-0054.1, 2020.